Published in final edited form as:

Dev Cell. 2023 November 06; 58(21): 2249–2260.e9. doi:10.1016/j.devcel.2023.08.007.

Mechanical stimulation from the surrounding tissue activates mitochondrial energy metabolism in *Drosophila* differentiating germ cells

Zong-Heng Wang[1], **Wenjing Zhao**[1], **Christian A. Combs**[1], **Fan Zhang**[1], **Jay R. Knutson**[1], **Mary A. Lilly**[2], **Hong Xu**[1,3,*]

[1]National Heart, Lung, and Blood Institute, National Institutes of Health, Bethesda, MD 20892, USA

[2]National Institute of Child Health and Human Development, National Institutes of Health, Bethesda, MD 20892, USA

[3]Lead contact

SUMMARY

In multicellular lives, the differentiation of stem cells and progenitor cells is often accompanied by a transition from glycolysis to mitochondrial oxidative phosphorylation. However, the underlying mechanism of this metabolic transition remains largely unknown. In this study, we investigate the role of mechanical stress in activating oxidative phosphorylation during differentiation of the female germline cyst in *Drosophila*. We demonstrate that the surrounding somatic cells flatten the 16-cell differentiating cyst, resulting in an increase of the membrane tension of germ cells inside the cyst. This mechanical stress is necessary to maintain cytosolic Ca^{2+} concentration in germ cells through a mechanically activated channel, Transmembrane channel-like. The sustained cytosolic Ca^{2+} triggers a CaMKI-Fray-JNK signaling relay, leading to the transcriptional activation of oxidative phosphorylation in differentiating cysts. Our findings demonstrate a molecular link between cell mechanics and mitochondrial energy metabolism, with implications in other developmentally orchestrated metabolic transitions in mammals.

Graphical Abstract

---

[*]Correspondence: Hong.Xu@nih.gov.

AUTHOR CONTRIBUTIONS

Conceptualization: Z.-H.W., H.X.; Investigation: Z.-H.W., C.C.; Methodology: Z.-H.W., C.C., W.Z., J.K.; Funding acquisition: J.K., M.L., H.X.; Project administration: Z.-H.W., H.X.; Supervision: Z.-H.W., M.L., H.X.; Data analysis: Z.-H.W., W.Z., F.Z.; Visualization: Z.-H.W., C.C., W.Z., H.X.; Writing - original draft: Z.-H.W., C.C., H.X.; Writing - review and editing: Z.-H.W., W.Z., M.L., H.X.

SUPPLEMENTAL INFORMATION

Supplemental Information contains seven figures, five videos, and two Tables.

DECLARATION OF INTERESTS

The authors declare no competing interests.

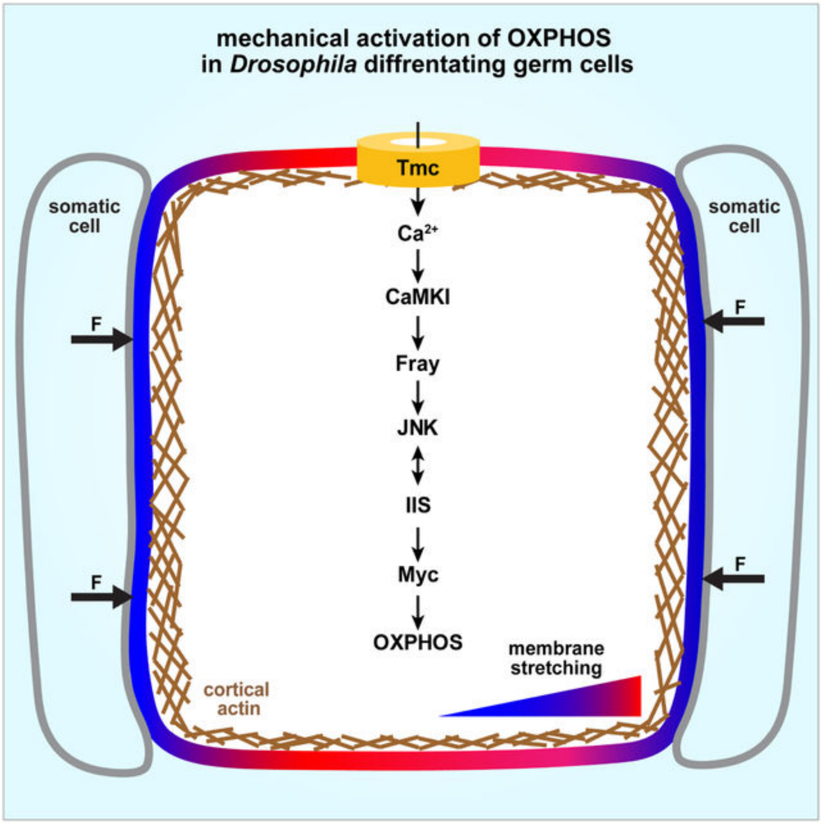

eTOC Blurb:

Wang et al. use *Drosophila* early oogenesis as a model to reveal how mitochondrial energy metabolism is induced during cell differentiation. They elucidate that mechanical stimulation from the surrounding tissue stretches the plasma membrane of differentiating germ cells, which induces mitochondrial energy metabolism through a Ca^{2+}-mediated signaling cascade.

INTRODUCTION

Mitochondria, the metabolic hub of cells, generate most cellular ATP through oxidative phosphorylation (OXPHOS) that is carried out by the electron transport chain (ETC).[1] Mitochondrial functions are subject to a dual genetic control. The mitochondrial genome, mtDNA, encodes 13 core subunits of the ETC. The majority of over 1000 mitochondrial proteins, including the remaining ETC subunits, factors essential for mtDNA replication and expression, and metabolic enzymes, are encoded by the nuclear genome.[2] Mitochondrial functions are fine-tuned by multifaceted transcriptional networks to accommodate energy and metabolic demands in different tissues and developmental processes.[3] Many types of stem cells and progenitor cells emphasize on glycolysis for ATP production, which preserves carbon sources for biosynthesis. However, during differentiation, cells switch to mitochondrial energy metabolism.[4,5] Defective OXPHOS impairs cell differentiation and is associated with various neuromuscular disorders and aging in both human and animal models.[4,6,7] Unicellular organisms can readily adjust energy metabolic programs in response to nutrient status and availability in the environment. However, stem cells and their differentiated progeny are subject to a same, controlled supply of nutrients from the circulation system[8]. The trigger for the transition in energy metabolism during cell differentiation in most developmental processes remains unclear.

Cell differentiation is often concomitant with cell migration or tissue morphogenesis.[9,10] As differentiating cells exit the stem cell niche and enter a new microenvironment, they establish interactions with the surrounding cells, leading to changes in cell mechanics. Extrinsic mechanical stimuli are sensed by mechanoresponsive machineries on the cell surface, such as mechanically activated ion channels, and are translated into various intracellular signaling.[11,12] Mechanical forces have emerged as key regulators of stem cell fate determination and tissue morphogenesis.[13–15] Ca^{2+} entry through Piezo, a mechanically activated ion channel, has been shown to regulate the renewal and differentiation of stem cells in both mammals and *Drosophila*.[16–18] The cytosolic Ca^{2+} concentration, which usually forms an oscillatory wave, is primarily regulated by processes that promote the entry of Ca^{2+} from the extracellular space and the release of Ca^{2+} from the endoplasmic reticulum (ER) into the cytosol, as well as counteractive actions that pump Ca^{2+} out of the cell or into the ER.[19,20] The elevated Ca^{2+} levels trigger cellular responses by activating Ca^{2+} binding proteins and their downstream signaling molecules, such as calmodulin and Calcium/Calmodulin-dependent kinases (CaMKs).[21,22] Interestingly, the overexpression of a constitutively active form of CaMKIV promotes mitochondrial DNA replication and increases the expression of mitochondrial enzymes in fatty acid metabolism and the electron transport chain, suggesting a Ca^{2+}-mediated regulation of mitochondrial biogenesis.[23] Nonetheless, a possible link between mechanical/Ca^{2+} signaling and metabolic transition in differentiating cells has yet to be explored.

Drosophila oogenesis provides an excellent model for studying mitochondrial biogenesis, energy metabolism, and their developmental regulations.[24–27] In the *Drosophila* ovary, a cystoblast produced by a germline stem cell undergoes four rounds of cell division with incomplete cytokinesis, resulting in a cyst of 16 interconnected germ cells (Figure 1A). At this stage, the cyst makes physical contact with a few pre-follicle cells (pFCs). The Delta ligand from the germline cyst activates Notch signaling in these pFCs, triggering their centripetal migration along the anterior surface of the cyst (Figures 1B and S1A).[28] These migrating pFCs, together with other pFCs, form a single-layered somatic epithelium that encases the germline cyst. Subsequently, the 16-cell cyst undergoes a transformation from a more rounded shape to a characteristic, one-cell thick lens shape and begins to differentiate (Figure 1A). The cyst, consisting of an oocyte and 15 nurse cells, eventually rounds up to form a sphere within the budding egg chamber.[29–31] OXPHOS is inactive in germ cells at earlier stages but is induced in differentiating cysts through a Myc-mediated transcriptional boost of both nuclear- and mtDNA-encoded ETC genes.[27] A transient increase in JNK activity in differentiating cysts activates Insulin/IGF-like signaling pathway (IIS) by increasing the transcription of Insulin-like receptor.[27] Activated IIS forms a feedforward loop with Myc, supporting ETC biogenesis and maintaining OXPHOS activity until the late stages of oogenesis (Figure 1C).[27]

The co-occurrence of pFC encapsulation and JNK activation in the differentiating cyst intrigued us to explore the potential role of interactions between cysts and pFCs in OXPHOS activation during cyst differentiation. In this study, we demonstrate that the surrounding pFCs flatten the differentiating cyst, increasing the tension of germ cells' plasma membrane. This process maintains cytosolic Ca^{2+} levels in germ cells via Transmembrane channel-like (Tmc), consequently activating OXPHOS through a CaMKI-Fray-JNK signaling relay.

RESULTS

pFC encapsulation triggers OXPHOS activation in flattened differentiating cysts

The inward migration of a few pFCs, called cross-migrating pFCs, is controlled by the germline-to-pFC Notch signaling.[28] To assess the contribution of pFC migration and encapsulation to OXPHOS activation in differentiating cysts, we inhibited pFC migration by conducting *Notch* RNA interference (RNAi) in follicle stem cell and pFCs using the *109–30-Gal4* driver (Figure S1B).[32] The inhibition of pFC migration through *Notch* RNAi resulted in the failure of cross-migrating pFCs to position themselves between germline cysts, while other pFCs maintained contact with the germline cysts (Figure S1C). This genetic manipulation did not appear to disrupt cyst differentiation, as the presence of 16-cell cysts containing differentiating oocytes marked with Orb was readily observed in the mid-germarium region (Figure S1D). However, both mitochondrial inner membrane potential ($\Delta\Psi m$) and cytochrome c oxidase (COX) activity were markedly reduced in rounded cysts (Figures 1D–1G). We next examined JNK activity using a *puc*-nLacZ reporter that expresses a nuclear-localized LacZ controlled by the endogenous promoter of *puc*, a target and a negative regulator of JNK.[33] *Notch* RNAi in pFCs resulted in a diminished *puc*-nLacZ signal in differentiating cysts (Figure 1H). Consistent with the notion that JNK triggers an IIS-Myc feedforward loop in differentiating cysts,[27] the protein level of Myc, visualized by endogenously expressed Myc-GFP, was markedly reduced in differentiating cysts, when cyst flattening was disrupted by pFC-specific *Notch* RNAi (Figure S1E). Additionally, the mRNA levels of Myc targets, including *Insulin-like Receptor* and nuclear-encoded *CoxIV*, and mtDNA-encoded *CoxIII*, were downregulated in these cysts (Figures S1F and S1G). Taken together, these results demonstrate that the envelopment of differentiating cysts by migrating pFCs is necessary for JNK-dependent OXPHOS activation.

pFC encapsulation increases the membrane tension of germ cells

The encapsulation of differentiating cysts by pFCs results in the flattening of cysts into a characteristic lens shape. However, when pFC migration was inhibited by *Notch* RNAi, the differentiating cysts remained rounded (Figures 1I, 1J, and S1C). Little cell growth was observed during the initial phase of cyst differentiation (Figure S2A). Transforming a sphere into an ellipsoid without changing its volume increases the surface area. Therefore, we hypothesized that cyst flattening would stretch the membrane and increase the membrane tension of germ cells in differentiating cysts. To this end, we performed fluorescence lifetime imaging microscopy (FLIM) on living ovaries labelled with Flipper-TR, a cell membrane tension reporter.[34] Increased membrane stretching enlarges the space between phospholipids tails, and in principle would allow Flipper-TR to adopt a trans-conformation that shortens its fluorescence lifetime.[34] To test Flipper-TR's properties in the fly ovary, we measured Flipper-TR lifetimes in germaria that were incubated in media with different osmolarity.[35] Compared to the isotonic medium, the hypotonic medium resulted in shortened Flipper-TR lifetimes on the germ cell membranes at various stages (Figures S2B–S2D). The most obvious change was observed in the germ cell membranes in the anterior region of the germaria (Figure S2B), presumably because they are more accessible to the medium. Consistent with this notion, the hypertonic medium led to greater Flipper-TR lifetimes on the germ cell membranes in that region but had little effect on cysts in the later stages (Figures S2B–S2D). Nonetheless, these results indicate an inverse correlation between Flipper-TR lifetime on the germ cell membrane and the degree of membrane stretching in the *Drosophila* ovary. Next, we compared Flipper-TR lifetimes between undifferentiated and differentiating cysts. In control germaria incubated in Schneider's medium, Flipper-TR lifetimes were similar at germ cell interfaces of undifferentiated cysts and the surfaces of both undifferentiated and differentiating cysts. However, the lifetimes were shorter at the germ cell interfaces in differentiating cysts (Figures 2A, 2B, S2B–S2F), suggesting that the plasma membrane at the germ cell interfaces, but not the cyst surface, is stretched during cyst differentiation.

Cell membrane is anchored to the underlying cortical actin cytoskeleton, which restricts the lateral diffusion of phospholipids in the membrane.[36,37] Using phalloidin staining, we observed that cortical actin was highly concentrated at the surface regions of differentiating cysts, but much less at the interfaces between germ cells, except at the ring canals (Figure 2C). When the differentiating cyst is flattened, the actin-enriched cortical region of the membrane may resist expansion and transmit forces to the interfaces between germ cells, resulting in membrane stretching at these regions (Figure 2D). Supporting this idea, inhibiting cyst flattening by pFC-specific *Notch* RNAi in fact led to a greater Flipper-TR lifetime at germ cell interfaces without affecting the density of cortical actin (Figures 2A, 2B, and S2E–S2H). These results indicate that pFC encapsulation flattens the differentiating cyst and thereby stretches a specific subregion of the germ cell membrane.

Membrane stretching regulates OXPHOS activation in differentiating cysts

To investigate the contribution of increased plasma membrane stretching to OXPHOS activation, we genetically manipulated membrane stretching and evaluated its effect on OXPHOS activities in differentiating cysts. Plasma membrane tension can be generated by the contraction of the cortical actomyosin network, which consists of the molecular motor non-muscle myosin II (NM II) and F-actin.[38] To inhibit cortical actomyosin contraction, we ectopically expressed Sqh^{A20A21}, a dominant negative mutant of Spaghetti squash (Sqh), the light chain subunit of the *Drosophila* NM II, in germ cells.[39] Overexpression of Sqh^{A20A21} reduced plasma membrane stretching (Figure S3). Importantly, both ΔΨm and COX activity were markedly reduced in differentiating cysts (Figure 3), indicating that increased membrane stretching is involved in OXPHOS activation. We further tested whether OXPHOS could be restored by increasing membrane stretching in differentiating cysts that lacked pFC encapsulation. To this end, we co-expressed a small hairpin RNA against *Delta*, the Notch ligand, and Sqh^{E20E21}, a constitutively active form of Sqh, in germ cells,[39] to inhibit the germline-to-pFC Notch signaling and to increase the cortical actomyosin contraction of germ cells, respectively. RNAi against *Delta* in germ cells phenocopied the effects of pFC-specific *Notch* RNAi, resulting in impaired pFC migration, rounded differentiating cysts, loss of membrane stretching at the germ cell interfaces, and reduced JNK and OXPHOS activities (Figures 1D–1J, S1C, S1D, and S3). Co-expression of Sqh^{E20E21} shortened Flipper-TR lifetime throughout the plasma membrane of germ cells with *Delta* RNAi, an indication of increased membrane stretching (Figure S3). Importantly, ectopically increasing cortical tension by Sqh^{E20E21} overexpression partially restored $\Delta\Psi$m and COX activity in these differentiating cysts (Figure 3). Taken together, these findings suggest that pFC encapsulation stretches germ cell membranes and this mechanical cue activates OXPHOS in differentiating cysts.

Tmc mediates OXPHOS activation in differentiating cysts through JNK

To further understand how the increased membrane tension activates OXPHOS, we performed a candidate germline RNAi screen targeting 40 genes annotated as “responsive to mechanical stimuli” for the phenotype of reduced COX activity in differentiating cysts (Supplemental Table S1). Tmc, a putative mechanically activated ion channel, emerged as the strongest hit. More than 80% germaria of flies with germline-specific *tmc* RNAi exhibited reduced COX activity (Figures S4A and S4B). Moreover, both COX activity and $\Delta\Psi$m were markedly decreased in the differentiating cysts of *tmc*^{1} (Figures 4A–4D), a null mutant of *tmc*.[40] Germline expression of a Tmc-Flag fusion protein restored COX activity and $\Delta\Psi$m in *tmc*^{1} differentiating cysts (Figures 4C–4F, and S4C), confirming that Tmc is required for OXPHOS activation. Next, we examined JNK activity in germaria using the *puc*-nLacZ reporter. In *tmc*^{1} differentiating cysts, the *puc*-nLacZ signal was significantly diminished, but was rescued by the expression of Tmc-Flag (Figure 4G). Importantly, ectopic activation of the JNK pathway by knocking down *puc* partially restored both COX activity and $\Delta\Psi$m in *tmc*^{1} differentiating cysts (Figures 4A–4D). These results demonstrate that Tmc acts upstream of JNK to activate OXPHOS in differentiating cysts.

Tmc maintains the concentrations of cytosolic Ca^{2+} in differentiating cysts

Mammalian TMC1, a member of mammalian TMC protein family, is a pore-forming protein of hair cell mechanoelectrical transducer channel and structurally related to hyperosmolality-gated calcium-permeable channels.[41,42] In *Drosophila*, Tmc is involved in modulating Ca^{2+} levels in response to mechanical forces in sensory neurons.[40,43] Therefore, we examined the potential impact of Tmc on cytosolic Ca^{2+} profile along germline cyst differentiation. We generated a UASz transgene that expresses a fusion protein consisted of mTagBFP2 and GCaMP6s linked by a self-cleaving P2A peptide (Figure 5A). GCaMP6s is a highly sensitive fluorescence Ca^{2+} reporter,[44] while mTagBFP2 serves as the internal control for GCaMP6s protein levels (Figure S5A). We generated a standard Ca^{2+} responsive curve for this ratiometric reporter using perfused S2 cells (Figure S5B). Simultaneous live imaging for both fluorescent proteins in control germaria revealed substantial variation in Ca^{2+} levels and Ca^{2+} oscillation patterns in germ cells at different developmental stages (Figures 5A and 5B). In control germaria, undifferentiated cysts exhibited the fastest Ca^{2+} oscillations and the highest basal cytosolic Ca^{2+} levels. As cysts differentiated, Ca^{2+} oscillations became slower, and basal cytosolic Ca^{2+} levels decreased compared to undifferentiated cysts. In budding egg chambers, the cytosolic Ca^{2+} level was the lowest, and no Ca^{2+} oscillation was observed during a 20-minute live imaging period (Figures 5C–5E, and Video S1). Knockdown of *tmc* in the germline did not significantly affect cytosolic Ca^{2+} level, the frequency and coefficient of variation of Ca^{2+} oscillations, or the properties of Ca^{2+} peaks in undifferentiated cysts (Figures S5C, S5E, S5F, S5H, S5J, S5K, and Video S2). Since *Tmc* transcript was uniformly expressed in the germarium (Figure S6), other mechanisms likely regulate Ca^{2+} levels and dynamics in germ cells at this stage. However, in differentiating cysts, *tmc* RNAi led to lower basal Ca^{2+} levels, while increased the frequency of Ca^{2+} oscillation with a smaller peak rise slope (Figures 5F–5H, S5D, S5G, S5I, S5J, S5K, and Video S2).

To further investigate which of these altered Ca^{2+} properties are related to OXPHOS defect in Tmc-depleted differentiating cysts, we expressed Parvalbumin (PV), a high-affinity Ca^{2+} binding protein,[45] to sequestrate free cytosolic Ca^{2+} in germ cells. Compared with *tmc* RNAi, PV expression led to a greater reduction in Ca^{2+} levels and nearly abolished Ca^{2+} oscillations in differentiating cysts, while impairing JNK and OXPHOS activity (Figures 5F–5H, S5C–S5K, S7A–S7E, and Video S3). Therefore, Tmc's role in maintaining cytosolic Ca^{2+} levels, rather than limiting Ca^{2+} oscillations, is required for JNK-dependent OXPHOS activation.

To investigate the impact of cyst flattening on the Ca^{2+} profile in germ cells, we co-expressed the Ca^{2+} reporter in germline cysts with *Delta* RNAi. Differentiating cysts with *Delta* RNAi showed reduced basal Ca^{2+} levels and increased Ca^{2+} oscillation frequency, similar to those with *tmc* RNAi (Figures 5F–5H, S5C–S5K, and Video S4). Additionally, overexpression of Sqh^{E20E21} restored the cytosolic Ca^{2+} levels in differentiating cysts with *Delta* RNAi (Figures 5F–5H, S5C–S5K, and Video S5). Together, these results suggest that Tmc-mediated Ca^{2+} entry in response to the stretching of the interface membranes is required for maintaining cytosolic Ca^{2+} levels in differentiating cysts. While mitochondrial Ca^{2+} is known to regulate OXPHOS and cell metabolism,[46] RNAi against MCU (the mitochondrial uniporter) did not have any notable impact on OXPHOS activation (Figures S7F–S7I), further supporting the role of cytosolic Ca^{2+} in OXPHOS activation during cyst differentiation.

Cytosolic Ca^{2+} mediates OXPHOS activation through CaMKI and Fray in differentiating cysts

Despite high level of cytosolic Ca^{2+}, OXPHOS remained inactive in undifferentiated cysts. We hypothesized that certain signaling molecules downstream of Ca^{2+} might be absent in undifferentiated cysts, thereby hindering OXPHOS activation. To this end, we assessed the potential involvement of genes associated with Ca^{2+} signaling and the JNK pathway in OXPHOS activation in differentiating cysts (Supplemental Table S2). Germline RNAi against CaMKI or Frayed, a conserved kinase regulating osmolarity responses,[47] abolished both OXPHOS and JNK activities in differentiating cysts (Figures 6A–6C, and S7J–S7L). Moreover, the reduction in OXPHOS activity observed in either *CaMKI* or *Fray* RNAi was partially restored by enhancing JNK activity through *puc* RNAi (Figures 5B, 5C, and S7J). This indicates that both CaMKI and Fray act upstream of JNK to activate OXPHOS during cyst differentiation. We observed that the expression of an endogenously tagged CaMKI-GFP fusion protein was low in early cysts but markedly increased in differentiating cysts and later stages (Figures 6D and 6E). In contrast, the expression of an endogenously tagged Fray-GFP fusion protein and *JNK* mRNA level remained consistent throughout cyst differentiation (Figures 6D, 6E, and S6). Noteworthy, the level of CaMKI-GFP remained normal in rounded differentiating cysts with germline *Delta* RNAi that disrupts the germline-to-pFC Notch signaling (Figures S7M and S7N). This suggests that while the flattening of differentiating cysts is necessary for sustaining Ca^{2+} levels, it is not required for the upregulation of CaMKI at this stage. Nonetheless, the increased abundance of CaMKI protein, combined with sufficient cytosolic Ca^{2+}, likely confers JNK activation specifically to differentiating cysts (Figure 6F).

Fray overexpression has been demonstrated to effectively activate its downstream targets,[48] which allowed us to determine the epistasis between Fray and other molecules identified in this study. We generated a UASz transgene expressing the Fray kinase (UASz-Fray-3HA). Overexpression of Fray enhanced both JNK activity and OXPHOS in differentiating cysts with *Tmc* RNAi or *CaMKI* RNAi (Figures 6A, 6C, 6G and S7O), suggesting that Ca^{2+} and CaMKI activate JNK and OXPHOS through Fray in differentiating cysts. Moreover, Fray overexpression also partially restored OXPHOS in rounded cysts resulting from germline *Delta* RNAi (Figures 6C and 6G). These findings further support the notion that the mechanical signaling triggered by cyst flattening activates OXPHOS during cyst differentiation (Figure 7).

DISCUSSION

A transition from glycolysis to OXPHOS is commonly observed during cell differentiation, but the underlying mechanism is largely unknown. The mechanical properties of differentiating cells are subject to changes in new microenvironment. Mechanical forces have emerged as key regulators controlling many developmental processes, such as stem cell fate determination, cell migration, and tissue morphogenesis.[13,14,49] In this study, using the model of *Drosophila* female germline cyst development, we uncover a previously unnoted role of mechanical stimuli in activating mitochondrial energy metabolism during cell differentiation (Figure 7). We assessed the changes in cell membrane stretching during cyst differentiation with the Flipper-TR probe and FLIM imaging. Colom and colleagues rationalized that an increase in the spaces between phospholipid tails or an expansion of cell membranes would reduce the lifetime of Flipper-TR.[34] In the *Drosophila* ovary, incubation with hypotonic medium reduced Flipper-TR lifetimes on germ cell membranes, in line with the proposed Flipper-TR working model. Similarly, overexpression of Sqh^{E20E21}, which increases cortical tension, shortened Flipper-TR lifetimes on germ cell membranes, further validating the property of Flipper-TR in the *Drosophila* ovary. We observed a reduction in the Flipper-TR lifetime in a restricted region, the interface membranes between the germ cells in differentiating cysts. The evidence that Flipper-TR lifetime could be influenced by the composition of phospholipids and their arrangement in the membrane may explain why hypotonic conditions that increase membrane tension resulted in longer Flipper-TR lifetimes in cultured mammalian cells.[34] It is not known that the composition of lipids or their orders are different between the germ cell interface membranes and the cyst surface. Hence, the reduction of Flipper-TR lifetime during cyst flattening most likely reflects an increase in membrane stretching at the interface regions. We propose that pressure from the surrounding pFCs, together with a lack of cortical actin meshwork that restricts the lateral movement of phospholipids, would stretch the membrane at germ cells interface and therefore increase the membrane tension therein.

Membrane tension can be sensed by a variety of transmembrane or membrane-associated proteins, including cytoskeletons, cell adhesion molecules, and mechanically activated ion channels. From our candidate screening for mechanoresponsive proteins involved in activating OXPHO in differentiating cysts, an evolutionary conserved mechanosensory channel, Tmc, was identified as the strongest hit. Differentiating cysts with *tmc* RNAi had lower basal cytosolic Ca^{2+} level but more frequent Ca^{2+} oscillations, phenocopying the rounded differentiating cysts with Delta RNAi. Importantly, ectopic activation of JNK or overexpression of Fray could restore COX activity in both tmc1 and delta RNAi differentiating cysts. These findings suggest that cyst flattening and Tmc function in the same pathway that activates OXPHO during cyst differentiation.

Tmc-dependent mechanosensation has been mainly studied in sensory neurons and muscles.[40,41,43,50–52] Mechanosensory neurons of *tmc* mutant lack Ca^{2+} influx upon mechanical stimuli,[40] indicating that Tmc, either alone or in conjunction with other proteins, can function as a Ca^{2+} channel. Therefore, the loss of tmc would lead to reduced Ca^{2+} influx in the differentiating cysts. Distinct gating mechanisms have been proposed for Tmc in different systems. Studies with green sea turtle TMC1 and budgerigar TMC2 reconstituted in liposomes have shown that these channels can be directly gated by pressure.[53] Indirect gating mechanisms have been proposed in mammals and *C. elegans*, where TMC proteins are linked to the extracellular matrix or actin cytoskeleton, respectively, through TMC binding proteins or tethers.[54,55] These tethers are believed to convey mechanical forces to open TMC channels. Given the functional conservation of *Drosophila* Tmc and the presence of fly homologs of Tmc tethers,[43] the tethering models of Tmc opening could also be possible. During tissue morphogenesis, Cadherin-based junctions link to cortical actin cytoskeleton and transduce tensional forces.[13,36] E-cadherin, which is present at the germ cell interfaces in differentiating cysts,[56,57] is one of the strongest hits from a previous candidate RNAi screen for defective COX activity.[37] This provides additional support for the tether model involving E-cadherin. In mammals, TMC1/2 are required for Ca^{2+} permeability of the MET channels.[51,58] However, whether TMC1/2 themselves mediate Ca^{2+} entry remains unclear. TMC proteins might influence the permeability of other Ca^{2+} channels. In line with this notion, our candidate RNAi screening also identified a few other Ca^{2+} channels, such as Trpγ and Piezo,[59–61] although the impact of RNAi of either gene on OXPHOS activation in differentiating cysts was less pronounced compared to *tmc* RNAi (Figure S4A). Further studies are necessary to determine whether Trpγ or Piezo acts in conjunction with Tmc to activate OXPHOS in differentiating cysts.

Mechanical activation of OXPHOS during *Drosophila* ovarian cyst differentiation shares similarities with neuronal differentiation in the mammalian cerebral cortex, where differentiating neurons migrate against mechanical barriers of the surrounding cells towards the cortical plate.[9] Both OXPHOS and JNK activities are elevated during neuronal differentiation.[62–65] Importantly, JNK inhibition downregulates the transcription of OXPHOS genes in differentiated neurons,[63] suggesting general implications of

JNK-mediated activation of OXPHOS in cell differentiation. Additionally, during the maturation of mammalian cardiomyocytes, increased Ca^{2+}-dependent contractility is associated with enhanced OXPHOS activity.[66,67] The contraction of cardiomyocytes is modulated by stretch-activated ion channels.[68] Several CaMK genes are upregulated during cardiomyocyte maturation.[69] Moreover, CaMKIV has been shown to promote the transcription of nuclear-encoded mitochondrial genes in mouse skeletal muscles.[23] Therefore, mechanical forces generated in developing tissues may function as developmental cues that trigger the spatiotemporal coupling of metabolic transition with cell differentiation and tissue development. Our work uncovers a molecular link between cell mechanics and mitochondrial energy metabolism and establishes a framework to further understand this conserved regulation in other developmental processes.

Limitations of the study

Inhibition of Tmc resulted in a decrease in the basal level of cytosolic Ca^{2+} but an increase in the frequency of Ca^{2+} oscillations in differentiating cysts. In sensory neurons, Tmc generates Ca^{2+} spikes lasting tens of seconds.[40] Given the diffusible nature of Ca^{2+} in the cytosol, Tmc-dependent Ca^{2+} influx could be readily equilibrated in germ cells that are interconnected within a cyst. Thus, it is puzzling that Tmc-depleted differentiating cysts exhibited sustained Ca^{2+}deficiency. It is possible that the reduced basal cytosolic Ca^{2+} level is a secondary effect of Ca^{2+} dysregulations resulting from impaired OXPHOS activation or endoplasmic reticulum-mitochondria interactions.[19] Additionally, the overexpression of Parvalbumin, which greatly reduced cytosolic Ca^{2+} levels and completely abolished Ca^{2+} oscillations, also impaired OXPHOS activation in differentiating cysts. We hence consider Tmc's role in maintaining cytosolic Ca^{2+} as essential for OXPHOS activation. Notably, some downstream targets of Ca^{2+} are sensitive to the frequency of Ca^{2+} spikes,[19] raising questions about the physiological consequences of increased Ca^{2+} oscillations in Tmc-depleted differentiating cysts that remain to be explored.

STAR★METHODS

RESOURCE AVAILABILITY

Lead contact—Further information and requests for reagents should be directed to and will be fulfilled by the Lead Contact, Hong Xu (Hong.Xu@nih.gov). Materials are available upon request.

Materials availability—All plasmids and transgenic lines generated in this study are available from the Lead Contact.

Data and code availability

- Original microscopy images and GraphPad files for quantifications were deposited at Mendeley (10.17632/6c46mnmkds.1).
- All data is publicly available as of the date of publication.
- Any additional information required to reanalyze the data reported in this paper is available from the Lead Contact upon request.

EXPERIMENTAL MODEL AND STUDY PARTICIPANT DETAILS

Fly genetics and husbandry—

Flies were maintained on standard BDSC cornmeal medium at 25°C. RNAi lines for candidate screen are listed in Supplemental Tables S1 and S2. *w*^{1118} (ctrl, BL3605), *Luciferase*-RNAi (ctrl, BL31603), *109–30*-Gal4 (*pFC-Gal4*, BL7023), *nos*-Gal4 (*germ-Gal4*, BL25751), *nos*-Gal4 (*germ-Gal4*, BL32563), UAS-2×EGFP (BL6874), *MTD*-Gal4 (germline, BL31777), *puc*-nLacZ (*puc*-lacZ$^{A251.1F3}$, BL11173), NRE-EGFP (BL30728), *Notch* RNAi (BL27988), *Delta* RNAi (BL36784), UASp-Sqh^{A20A21} (BL64114), UASp-Sqh^{E20E21} (BL64411), *tmc*^{1} (BL66556),[40] *tmc* RNAi (BL50984), *puc* RNAi (BL36085), *JNK* RNAi (BL31323), *MCU* RNAi (BL67857), *CaMKI* RNAi (BL35362), *CaMKI* RNAi #2 (BL41900), *fray* RNAi (BL42569), *fray* RNAi #2 (BL55878), and Myc-GFP (BL81274) were obtained from Bloomington Drosophila Stock Center. CaMKI-GFP (v318349) and Fray-GFP (v318460) were from Vienna Drosophila Resource Center.

Transgenic flies—

To generate pUASz-mTagBFP2-P2A-GCaMP6s and pUASz-mTagBFP2, GCaMP6s was amplified from pGP-CMV-GCaMP6s (#40753, addgene) and mTagBFP2 from pCAG-mTagBFP2.[44,71] GCaMP6s and mTagBFP2, as well as a P2A fragment (GCCACCAACTTCTCCCTGCTGAAGCAGGCCGGCGACGTGGAGGAGAACCC-CGGCCCC), and an mTagBFP2 fragment alone, were subcloned into XhoI-cut UASZ-1.0,[72] respectively, with the In-Fusion HD Cloning kit (639650, Takara Bio Inc.). The Parvalbumin (PV) DNA fragment and the coding region of Fray were amplified from pCMV-PV-GFP (#17301, addgene) and RE53265 (BDGP cDNA library), respectively. Plasmid containing full-length of *Drosophila* Tmc was a kind gift from Dr. Craig Montell. A 3×HA tag was added to the C-terminal of PV and Fray, respectively, and a Flag tag was added to the C-terminal of Tmc, all of which were subcloned into XhoI-cut UASZ-1.0 with the In-Fusion Cloning kit. Transgenic flies carrying these constructs were generated by Bestgene Inc.

METHOD DETAILS

Morphological analysis of female germline cysts in 3D—

Z-stack images were opened with Imaris (version 9.7, Oxford Instruments). Individual 16-cell cysts were identified based on DAPI staining. In germaria with somatic *N* RNAi or germline *Delta* RNAi, fused cysts were observed in some budding egg chambers. We only analyzed the shape of budding egg chamber cysts with 16 cells. In Imaris, 3D surface view of individual germline cyst was generated with the 'surfaces' tool. 'Draw' was used to manually trace the same cyst in each confocal step. After generating 3D surfaces with 'create surface', the values of cyst sphericity, ellipticity (oblate), and size were obtained in 'detailed statistics'. Images of 3D surfaces were generated with 'snapshot'.

Immunofluorescence staining—

Immunofluorescence staining was performed as previously described.[27] For immunofluorescence staining, antibodies/dye used were as follows: rabbit anti-Vasa (1:1000, sc-30210, Santa Cruz Biotechnology), rabbit anti-GFP (1:1,000, NB600–308, Novus Biologicals); mouse anti-Orb (1:800, 6H4, Developmental Studies Hybridoma Bank); mouse anti-Hts (1:800, 1B1, Developmental Studies Hybridoma Bank); mouse anti-β-galactosidase (1:1200, Z378A, Promega); mouse anti-FLAG (1:1000, F1804, MilliporeSigma); Alexa Fluor 568-Phalloidin (1:500, A12380, Invitrogen); Alexa Fluor 568 donkey anti-rabbit IgG (1:600, A10042, Invitrogen), Alexa Fluor 568 goat anti-mouse IgG (1:600, A11004, Invitrogen), Alexa Fluor 488 goat anti-rabbit IgG (1:600, A11034, Invitrogen), and Alexa Fluor 488 goat anti-mouse IgG (1:600, R37120, Invitrogen).

Samples were mounted with Vectashield mounting medium with DAPI (H-1500, Vector Laboratories). Confocal images of germaria were collected on a Perkin Elmer Ultraview system (Zeiss Plan-apochromat 63×/1.4 oil lens, Volocity software, Hamamatsu Digital Camera C10600 ORCA-R2, Immersol immersion oil 518F) with a 0.3 μm step size. Images for morphological analysis of female germline cysts were acquired with an Instant Sim (iSIM) Super-Resolution Microscope (Olympus UPlanSApo 60×/1.30 Sil lens, Metamorph acquisition software, ORCA-Flash4.0 V2 Digital CMOS camera C11440, Silicone Immersion Oil SIL300CS-30SC) with a 0.2 μm step size. All confocal images were processed with NIH ImageJ (National Institutes of Health).

Fluorescence in situ hybridization (FISH)—Fluorescently (Quasar® 570) labeled Stellaris FISH probes against *CoxIV*, *CoxIII*, *InR*, *Tmc*, and *JNK* mRNA were synthesized by Biosearch Technologies. DNA sequences for the *Tmc* and *JNK* probes are listed in KEY RESOURCES TABLE, while DNA sequences for the *CoxIV*, *CoxIII* and *InR* probes were published in our previous study.[27] FISH on *Drosophila* ovaries were performed according to a published protocol.[73] Briefly, dissected ovaries were fixed in 4% PFA in PBS for 20 min. After 5×5 min in washes with PBST (PBS and 0.2% Triton X-100), ovaries were permeabilized with 3 μg/ml proteinase K in PBS on ice for 1 h. Permeabilization was stopped by incubating ovaries in PBS with 20 mg/ml glycine and was followed by a post-fixation in PBST with 4% PFA for 20 min. After 5×2 min washes with PBST, ovaries were incubated in prehybridization solution (2× SSC and 10% formamide) at room temperature for 10 min. Prehybridization solution was removed, and 60 μl of hybridization solution (6 μl deionized formamide, 3 μg heparin, 1 μl salmon sperm DNA, 80 ng probe mix, 6 μg dextran sulfate, 120 μg BSA, and 5 μl of 20× SSC) was added. Ovaries were protected from light and incubated at 37°C overnight. Ovaries were then washed for 3×15 min with prewarmed prehybridization solution in at 37°C, followed by 4×5 min washes with PBS at room temperature. Z-stack images with smFISH, mTagBFP2, and nuclear (DAPI) channels were collected with the Perkin Elmer Ultraview system (Zeiss Plan-apochromat 63×/1.4 oil lens, Volocity software, Hamamatsu Digital Camera C10600 ORCA-R2, Immersol immersion oil 518F) or the iSIM Super-Resolution Microscope (Olympus UPlanSApo 60×/1.30 Sil lens, Metamorph acquisition software, ORCA-Flash4.0 V2 Digital CMOS camera C11440, Silicone Immersion Oil SIL300CS-30SC) and processed with NIH ImageJ.

Calcium imaging and analyses—Three-day-old females were collected. Their ovaries were dissected in Schneider's medium (Thermo Fisher Scientific) and immerged in hydrogel as adapted from a previous study.[57] Briefly, dissected ovaries were transferred into a droplet of medium on a 22×22 mm coverslip that were previously coated with 3-(trimethoxysilyl) propyl methacrylate (440159, Sigma Aldrich). Medium was then replaced by 15 μl of 10% PEG-DA hydrogel solution (GS700, Advanced BioMatrix, Inc.) with 0.1% Irgacure 2959 (photo initiator, 410896, Sigma-Aldrich). A coverslip treated with deperlent was placed above the hydrogel solution. The coverslip/coverslip sandwich was illuminated by a UV light source for 30 s at 312 nm for gelation. Then, the upper coverslip was removed and the bottom coverslip with the hydrogel was placed into a Chamlide chamber (CM-S22–1, Quorum Technologies) filled with Schneider's medium. Time-lapse imaging (every 5 s for 20 min) of the middle section (z-axis) of the germarium was performed on a Leica SP8 confocal microscope (HC PL APO CS2 63×/1.40 N.A. objective lens) using the Las X software (version 3.5.7). Fluorescence of GCaMP6s (excitation: 488 nm, emission: 500–550 nm, and gain: 150%) and mTagBFP2 (excitation: 405 nm, emission at 440–480 nm, and gain: 0%) were recorded simultaneously as videos at 8-bit depth.

The video flies were opened with NIH ImageJ. 'Freehand selections' was used to select germ cell areas. Time-lapse fluorescence intensities for both channels in individual germ cells were obtained with 'plot z-axis profile'. Time-lapse background intensity of each channel calculated from a 10×10 μm^2 square outside the germarium was subtracted from the time-lapse fluorescence intensities. Time-lapse ratios of GCaMP6s/mTagBFP2 intensities were imported into Origin 2021 (OriginLab Corporation). In Origin 2021, Ca^{2+} oscillations in each germ cell during the 20-min recording were counted manually based on the individual peaks of GCaMP6s/mTagBFP2 intensity ratio. In Excel, average Ca^{2+} level for each germ cell was calculated by averaging the fluorescence ratio of the 20-min imaging. The baseline Ca^{2+} level between oscillations was calculated by averaging the ratio without the peaks. Coefficient of variation is defined by the standard deviation of peak periods of Ca^{2+} oscillations divided by the mean and expressed as a percentage.[74] Peak periods from individual germ cells were measured in Origin 2021. Mean and the standard deviation of peak periods was calculated to obtain coefficient of variation in Excel.

For Ca^{2+} calibration, the mTagBFP2-P2A-GCaMP6s fragment was firstly subcloned into the pIB/V5-His vector (V802001, Invitrogen) with the In-Fusion Cloning kit. 2×10^6 S2 cells (S2-DRSC, *Drosophila* Genomics Resource Center) were seeded in a 60 mm dish and transfected with 2 μg the pIB-mTagBFP2-P2A-GCaMP6s-V5-His construct using Effectene Transfection Reagent (Qiagen). After 2 days, cells were spread on concanavalin A-coated chambered coverglasses (155411, Thermo Scientific) and permeabilized by 150 μM digitonin (D141, Sigma-Aldrich) in the zero free calcium buffer (30 mM MOPS, pH 7.2, 100 mM KCl, 10 mM EGTA; see below) for 10 min. A series of buffers with 11 different free calcium concentrations were obtained by mixing the zero free calcium buffer (30 mM MOPS, pH 7.2, 100 mM KCl, 10 mM EGTA) and the 39 μM free calcium buffer (30 mM MOPS, pH 7.2, 100 mM KCl, 10 mM CaEGTA) in various ratios (Calcium Calibration Buffer Kit #1, Life Technologies) and added to different wells of chambered coverglasses. Confocal images of transfected cells (n = 13~29 cells for each calcium concentration) were acquired by a Leica SP8 confocal microscope (HC PL APO CS2 63x/1.40 N.A. objective lens) using the Las X software with the same settings for Ca^{2+} imaging on germaria. In Prism 9 (GraphPad), background removed ratios of GCaMP6s/mTagBFP2 intensities were plotted to generate a sigmoidal standard curve that was then utilized to fit the germ cell data.

Membrane tension measurements—Cell membrane tension was measured with Flipper-TR fluorescent tension probe (SC020, Cytoskeleton, Inc.).[34] Dissected ovaries were incubated with 2 μM Flipper-TR in Schneider's medium for 30 min. Single z-plane FLIM images of the germarium regions were acquired using a Leica SP8 Falcon FLIM confocal microscope, a HC PL APO CS2 63×/1.40 N.A. objective lens, and Leica Las X. Point scanning excitation at a speed of 400 Hz was performed at 488 nm using a pulsed white-light laser operating at 80 MHz with emission collected over a bandwidth of 550–650 nm onto a hybrid single molecule detector (HyD SMD) at 16-bit digitization with a pinhole set to 1 A.U. Image size was set to 512×512 pixels^2 with pixel sizes of 300 nm. Fluorescence from germaria as frame accumulated over 70 images to build up an adequate number of photons per pixel for further analysis. Time-correlated single photon counting histograms were collected with 136 channels in a 13 ns time window (97 ps per channel). Before lifetime fitting, pixel binning of 2 was performed to provide peak counts of at least 600 photons/pixel for the dual exponential fits, followed by a manual thresholding to omit background pixels. Fluorescence decay data from full images was fitted to a dual exponential tail fit model in the Las X software. Images of the longest lifetime were exported for further analysis. A custom program written in IDL (Interactive Data Language, L3Harris Geospatial) was used to obtain average lifetime values in regions of interest (ROIs) from the lifetime pixel-map images generated by the Las X software.

For osmotic shock experiments, isotonic, hypotonic, and hypertonic media were prepared as previously described.[75] Briefly, isotonic medium was made by mixing *Drosophila* saline (15 mM HEPES pH 7.0, 117.5 mM NaCl, 20 mM KCl, 8.5 mM $MgCl_2$, 2 mM $CaCl_2$, 10.2 mM $NaHCO_3$, 4.3 mM NaH_2PO_4, and 20 mM glucose) and Schneider's medium at a 1:1 ratio. Hypotonic saline was obtained by mixing isotonic medium and H_2O at a ratio of 10:3. Hypertonic saline was a modified isotonic medium containing 0.1 M sucrose. Ovaries were dissected, equilibrated for 60 min, incubated with 2 μM Flipper-TR for 20 min, and imaged in each medium, respectively.

COX activity histochemistry—Histochemical activity staining and quantification for cytochrome c oxidase (complex IV) were performed according to the procedure from our previous study.[27] Four to eight pairs of ovaries from 2~3-day-old flies were dissected in PBS and ovarioles were separated by using a dissection needle. Ovaries were incubated with COX staining solution [50 mM phosphate solution (pH 7.4), 4 mM 3,3'-diaminobenzidine, 2 μg/ml catalase, 200 μM cytochrome c, 4 mM antimycin A, 84 mM malonate, and 60 μM rotenone] for 30 min at room temperature. For negative control, ovaries (*Luciferase* RNAi) were treated with 2 mM KCN in COX staining solution for 30 min at room temperature. Negative control was performed with each batch of COX activity staining. All reactions were followed by 2×5 min washes with phosphate solution and 4% paraformaldehyde fixation for 15 mins. After 2×5 min washes in phosphate solution, ovaries were immersed in 80% glycerol in phosphate solution. Brightfield images of germaria were collected by a Zeiss Axio Observer Z1 microscope (C-Apochromat 40×/1.1 W Corr objective lens for ovaries).

Relative ETC activities in differentiating cysts were quantified with ImageJ. From the opened images, areas of differentiating cysts were isolated with 'freehand selections' and followed by 'clear outside'. The color of the cysts was converted into gray and inverted to obtain images with black background. The COX staining area was selected with 'color threshold'. Mean intensity of the selected COX staining area was measured. Mean intensity of non-selected area was considered as background and subtracted from the mean intensity of selected area. From each batch of activity staining, relative COX activity of ctrl differentiating cysts was considered as ‘1’, while the intensity from the negative control was considered as ‘0’ activity.

Mitochondrial membrane potential staining—Ovaries were dissected in Schneider’s medium with 10% fetal bovine serum and incubated with medium containing TMRM (20 nM, I34361, Thermo Fisher Scientific) and MitoTracker Green (100 nM, M7514, Invitrogen) for 20 min. The ovaries were then rinsed three times with PBS and imaged alive within 40 min on a PerkinElmer Ultraview system (Zeiss Plan-apochromat 63×/1.4 oil lens, Volocity acquisition software, Hamamatsu Digital Camera C10600 ORCA-R2, Immersol immersion oil).

To acquire ratiometric TMRM/MitoTracker Green images, z-stack images (3 steps with 0.4 μm/z-step) were opened in ImageJ. TMRM and MitoTracker Green channels were separated. Regions of mitochondria were chosen in the MitoTracker Green image with the “color threshold” function at default settings. “Restore selection” function was applied to outline mitochondria in the corresponding TMRM image. Fluorescence outside mitochondria was removed from either channel with “clear outside” function. The ratiometric images were generated with “Image Calculator” function by normalizing the intensity of TMRM with that of MitoTracker Green. Mean TMRM and MitoTracker Green intensities of the germline mitochondria were measured. From either channel, mean intensity of non-selected areas was considered as background and subtracted from the mean intensity of germline mitochondria. The ratio between TMRM and MitoTracker Green intensity was obtained by dividing the value of TMRM intensity by that of MitoTracker Green intensity. From each batch of staining, relative TMRM/MitoTracker Green ratio of ctrl differentiating cysts was normalized as ‘1’.

QUANTIFICATION AND STATISTICAL ANALYSIS

Sample size was not predetermined by statistical methods. The experiments were not randomized. Investigators were not blinded. Prism 9 (GraphPad) was used to plot data and perform statistical analyses. Error bars in all charts represent standard errors. Mann-Whitney test (two-tailed) was used to determine the mean differences between two unpaired groups, and Wilcoxon signed-rank test (two-tailed) for the differences between two paired groups. Kruskal-Wallis test, followed by Dunn’s multiple comparisons test, was performed to compare three and more groups. Differences were considered statistically significant when $P < 0.05$.

Supplementary Material

Refer to Web version on PubMed Central for supplementary material.

ACKNOWLEDGEMENTS

We thank F. Chanut for comments and editing on the manuscript; the Bloomington Drosophila Stock Center and the Vienna Drosophila Resource Center for providing fly lines; the Developmental Studies of Hybridoma Bank for various antibodies; Bestgene Inc. for Drosophila transgenesis service. This work is supported by the National Heart

Lung and Blood Institute Intramural Research Program and the Eunice Kennedy Shriver National Institute of Child Health and Human Development Intramural Research Program.

INCLUSION AND DIVERSITY

We support inclusive, diverse, and equitable conduct of research.

REFERENCES

1. Spinelli JB, and Haigis MC (2018). The multifaceted contributions of mitochondria to cellular metabolism. Nature Cell Biology 20, 745–754. 10.1038/s41556-018-0124-1. [PubMed: 29950572]
2. Chen Z, Zhang F, and Xu H (2019). Human mitochondrial DNA diseases and Drosophila models. J Genet Genomics 46, 201–212. 10.1016/j.jgg.2019.03.009. [PubMed: 31076279]
3. Dominy JE, and Puigserver P (2013). Mitochondrial Biogenesis through Activation of Nuclear Signaling Proteins. Csh Perspect Biol 5. 10.1101/cshperspect.a015008
4. Xu X, Duan S, Yi F, Ocampo A, Liu GH, and Izpisua Belmonte JC (2013). Mitochondrial regulation in pluripotent stem cells. Cell Metab 18, 325–332. 10.1016/j.cmet.2013.06.005. [PubMed: 23850316]
5. Shyh-Chang N, and Ng HH (2017). The metabolic programming of stem cells. Genes Dev 31, 336–346. 10.1101/gad.293167.116. [PubMed: 28314766]
6. Zhang F, Pirooznia M, and Xu H (2020). Mitochondria regulate intestinal stem cell proliferation and epithelial homeostasis through FOXO. Molecular Biology of the Cell 31, 1538–1549. 10.1091/mbc.E19-10-0560. [PubMed: 32374658]
7. Davie K, Janssens J, Koldere D, De Waegeneer M, Pech U, Kreft L, Aibar S, Makhzami S, Christiaens V, Gonzalez-Blas CB, et al. (2018). A Single-Cell Transcriptome Atlas of the Aging Drosophila Brain. Cell 174, 982–998. 10.1016/j.cell.2018.05.057. [PubMed: 29909982]
8. Vander Heiden MG, Cantley LC, and Thompson CB (2009). Understanding the Warburg effect: the metabolic requirements of cell proliferation. Science 324, 1029–1033. 10.1126/science.1160809. [PubMed: 19460998]
9. Javier-Torrent M, Zimmer-Bensch G, and Nguyen L (2021). Mechanical Forces Orchestrate Brain Development. Trends in Neurosciences 44, 110–121. 10.1016/j.tins.2020.10.012. [PubMed: 33203515]
10. Li HJ, and Jasper H (2016). Gastrointestinal stem cells in health and disease: from flies to humans. Dis Model Mech 9, 487–499. 10.1242/dmm.024232. [PubMed: 27112333]
11. Jaalouk DE, and Lammerding J (2009). Mechanotransduction gone awry. Nat Rev Mol Cell Bio 10, 63–73. 10.1038/nrm2597. [PubMed: 19197333]
12. Martino F, Perestrelo AR, Vinarsky V, Pagliari S, and Forte G (2018). Cellular Mechanotransduction: From Tension to Function. Front Physiol 9. 10.3389/fphys.2018.00824.
13. Heisenberg CP, and Bellaiche Y (2013). Forces in Tissue Morphogenesis and Patterning. Cell 153, 948–962. 10.1016/j.cell.2013.05.008. [PubMed: 23706734]
14. Vining KH, and Mooney DJ (2017). Mechanical forces direct stem cell behaviour in development and regeneration. Nat Rev Mol Cell Bio 18, 728–742. 10.1038/nrm.2017.108. [PubMed: 29115301]
15. Handler A, and Ginty DD (2021). The mechanosensory neurons of touch and their mechanisms of activation. Nat Rev Neurosci 22, 521–537. 10.1038/s41583-021-00489-x. [PubMed: 34312536]
16. Pathak MM, Nourse JL, Tran T, Hwe J, Arulmoli J, Le DTT, Bernardis E, Flanagan LA, and Tombola F (2014). Stretch-activated ion channel Piezo1 directs lineage choice in human neural stem cells. P Natl Acad Sci USA 111, 16148–16153. 10.1073/pnas.1409802111.
17. He L, Si G, Huang JH, Samuel ADT, and Perrimon N (2018). Mechanical regulation of stem-cell differentiation by the stretch-activated Piezo channel. Nature 555, 103–106. 10.1038/nature25744. [PubMed: 29414942]
18. Ranade SS, Syeda R, and Patapoutian A (2015). Mechanically Activated Ion Channels. Neuron 87, 1162–1179. 10.1016/j.neuron.2015.08.032. [PubMed: 26402601]

19. Dupont G, and Combettes L (2016). Fine tuning of cytosolic Ca^{2+} oscillations. F1000Res 5. 10.12688/f1000research.8438.1.
20. Woll KA, and Van Petegem F (2022). Calcium-release channels: structure and function of IP(3) receptors and ryanodine receptors. Physiol Rev 102, 209–268. 10.1152/physrev.00033.2020. [PubMed: 34280054]
21. Clapham DE (2007). Calcium signaling. Cell 131, 1047–1058. 10.1016/j.cell.2007.11.028. [PubMed: 18083096]
22. Bootman MD (2012). Calcium signaling. Cold Spring Harb Perspect Biol 4, a011171. 10.1101/cshperspect.a011171. [PubMed: 22751152]
23. Wu H, Kanatous SB, Thurmond FA, Gallardo T, Isotani E, Bassel-Duby R, and Williams RS (2002). Regulation of mitochondrial biogenesis in skeletal muscle by CaMK. Science 296, 349–352. 10.1126/science.1071163. [PubMed: 11951046]
24. Teixeira FK, Sanchez CG, Hurd TR, Seifert JRK, Czech B, Preall JB, Hannon GJ, and Lehmann R (2015). ATP synthase promotes germ cell differentiation independent of oxidative phosphorylation. Nature Cell Biology 17, 689–696. 10.1038/ncb3165. [PubMed: 25915123]
25. Sieber MH, Thomsen MB, and Spradling AC (2016). Electron Transport Chain Remodeling by GSK3 during Oogenesis Connects Nutrient State to Reproduction. Cell 164, 420–432. 10.1016/j.cell.2015.12.020. [PubMed: 26824655]
26. Zhang Y, Wang ZH, Liu Y, Chen Y, Sun N, Gucek M, Zhang F, and Xu H (2019). PINK1 Inhibits Local Protein Synthesis to Limit Transmission of Deleterious Mitochondrial DNA Mutations. Mol Cell 73, 1127–1137. 10.1016/j.molcel.2019.01.013. [PubMed: 30772175]
27. Wang ZH, Liu Y, Chaitankar V, Pirooznia M, and Xu H (2019). Electron transport chain biogenesis activated by a JNK-insulin-Myc relay primes mitochondrial inheritance in Drosophila. Elife 8. 10.7554/eLife.49309.
28. Nystul T, and Spradling A (2010). Regulation of epithelial stem cell replacement and follicle formation in the Drosophila ovary. Genetics 184, 503–515. 10.1534/genetics.109.109538. [PubMed: 19948890]
29. Rust K, and Nystul T (2020). Signal transduction in the early Drosophila follicle stem cell lineage. Current Opinion in Insect Science 37, 39–48. 10.1016/j.cois.2019.11.005. [PubMed: 32087562]
30. Huynh JR, and Johnston DS (2004). The origin of asymmetry: Early polarisation of the Drosophila germline cyst and oocyte. Current Biology 14, R438–R449. 10.1016/j.cub.2004.05.040. [PubMed: 15182695]
31. de Cuevas M, Lilly MA, and Spradling AC (1997). Germline cyst formation in Drosophila. Annual Review of Genetics 31, 405–428. 10.1146/annurev.genet.31.1.405.
32. Hartman TR, Zinshteyn D, Schofield HK, Nicolas E, Okada A, and O'Reilly AM (2010). Drosophila Boi limits Hedgehog levels to suppress follicle stem cell proliferation. J Cell Biol 191, 943–952. 10.1083/jcb.201007142. [PubMed: 21098113]
33. Martin-Blanco E, Gampel A, Ring J, Virdee K, Kirov N, Tolkovsky AM, and Martinez-Arias A (1998). puckered encodes a phosphatase that mediates a feedback loop regulating JNK activity during dorsal closure in Drosophila. Genes Dev 12, 557–570. 10.1101/gad.12.4.557. [PubMed: 9472024]
34. Colom A, Derivery E, Soleimanpour S, Tomba C, Dal Molin M, Sakai N, Gonzalez-Gaitan M, Matile S, and Roux A (2018). A fluorescent membrane tension probe. Nature Chemistry 10, 1118–1125. 10.1038/s41557-018-0127-3.
35. Sun Q, Wu Y, Jonusaite S, Pleinis JM, Humphreys JM, He H, Schellinger JN, Akella R, Stenesen D, Kramer H, et al. (2018). Intracellular Chloride and Scaffold Protein Mo25 Cooperatively Regulate Transepithelial Ion Transport through WNK Signaling in the Malpighian Tubule. J Am Soc Nephrol 29, 1449–1461. 10.1681/ASN.2017101091. [PubMed: 29602832]
36. Sitarska E, and Diz-Munoz A (2020). Pay attention to membrane tension: Mechanobiology of the cell surface. Curr Opin Cell Biol 66, 11–18. 10.1016/j.ceb.2020.04.001. [PubMed: 32416466]
37. Lenne PF, Wawrezinieck L, Conchonaud F, Wurtz O, Boned A, Guo XJ, Rigneault H, He HT, and Marguet D (2006). Dynamic molecular confinement in the plasma membrane by microdomains and the cytoskeleton meshwork. Embo J 25, 3245–3256. 10.1038/sj.emboj.7601214. [PubMed: 16858413]

38. Lecuit T, Lenne PF, and Munro E (2011). Force generation, transmission, and integration during cell and tissue morphogenesis. Annu Rev Cell Dev Biol 27, 157–184. 10.1146/annurev-cellbio-100109-104027. [PubMed: 21740231]
39. Winter CG, Wang B, Ballew A, Royou A, Karess R, Axelrod JD, and Luo L (2001). Drosophila Rho-associated kinase (Drok) links Frizzled-mediated planar cell polarity signaling to the actin cytoskeleton. Cell 105, 81–91. 10.1016/S0092-8674(01)00298-7. [PubMed: 11301004]
40. Zhang YV, Aikin TJ, Li Z, and Montell C (2016). The Basis of Food Texture Sensation in Drosophila. Neuron 91, 863–877. 10.1016/j.neuron.2016.07.013. [PubMed: 27478019]
41. Pan BF, Akyuz N, Liu XP, Asai Y, Nist-Lund C, Kurima K, Derfler BH, Gyorgy B, Limapichat W, Walujkar S, et al. (2018). TMC1 Forms the Pore of Mechanosensory Transduction Channels in Vertebrate Inner Ear Hair Cells. Neuron 99, 736–753. 10.1016/j.neuron.2018.07.033. [PubMed: 30138589]
42. Akyuz N, Karavitaki KD, Pan B, Tamvakologos PI, Brock KP, Li Y, Marks DS, and Corey DP (2022). Mechanical gating of the auditory transduction channel TMC1 involves the fourth and sixth transmembrane helices. Sci Adv 8, eabo1126. 10.1126/sciadv.abo1126. [PubMed: 35857511]
43. Guo YM, Wang YP, Zhang W, Meltzer S, Zanini D, Yu Y, Li JF, Cheng T, Guo ZH, Wang QX, et al. (2016). Transmembrane channel-like (tmc) gene regulates Drosophila larval locomotion. P Natl Acad Sci USA 113, 7243–7248. 10.1073/pnas.1606537113.
44. Chen TW, Wardill TJ, Sun Y, Pulver SR, Renninger SL, Baohan A, Schreiter ER, Kerr RA, Orger MB, Jayaraman V, et al. (2013). Ultrasensitive fluorescent proteins for imaging neuronal activity. Nature 499, 295–300. 10.1038/nature12354. [PubMed: 23868258]
45. Pusl T, Wu JJ, Zimmerman TL, Zhang L, Ehrlich BE, Berchtold MW, Hoek JB, Karpen SJ, Nathanson MH, and Bennett AM (2002). Epidermal growth factor-mediated activation of the ETS domain transcription factor Elk-1 requires nuclear calcium. J Biol Chem 277, 27517–27527. 10.1074/jbc.M203002200. [PubMed: 11971908]
46. Rossi A, Pizzo P, and Filadi R (2019). Calcium, mitochondria and cell metabolism: A functional triangle in bioenergetics. Biochim Biophys Acta Mol Cell Res 1866, 1068–1078. 10.1016/j.bbamcr.2018.10.016. [PubMed: 30982525]
47. Rodan AR, and Jenny A (2017). WNK Kinases in Development and Disease. Curr Top Dev Biol 123, 1–47. 10.1016/bs.ctdb.2016.08.004. [PubMed: 28236964]
48. Sato A, and Shibuya H (2013). WNK signaling is involved in neural development via Lhx8/Awh expression. PLoS One 8, e55301. 10.1371/journal.pone.0055301. [PubMed: 23383144]
49. Ladoux B, and Mege RM (2017). Mechanobiology of collective cell behaviours. Nat Rev Mol Cell Bio 18, 743–757. 10.1038/nrm.2017.98. [PubMed: 29115298]
50. Vreugde S, Ereven A, Kros CJ, Marcotti W, Fuchs H, Kurima K, Wilcox ER, Friedman TB, Griffith AJ, Balling R, et al. (2002). Beethoven, a mouse model for dominant, progressive hearing loss DFNA36. Nat Genet 30, 257–258. 10.1038/ng848. [PubMed: 11850623]
51. Pan BF, Geleoc GS, Asai Y, Horwitz GC, Kurima K, Ishikawa K, Kawashima Y, Griffith AJ, and Holt JR (2013). TMC1 and TMC2 Are Components of the Mechanotransduction Channel in Hair Cells of the Mammalian Inner Ear. Neuron 79, 504–515. 10.1016/j.neuron.2013.06.019. [PubMed: 23871232]
52. He LP, Gulyanon S, Skanata MM, Karagyozov D, Heckscher ES, Krieg M, Tsechpenakis G, Gershow M, and Tracey WD (2019). Direction Selectivity in Drosophila Proprioceptors Requires the Mechanosensory Channel Tmc. Current Biology 29, 945–956. 10.1016/j.cub.2019.02.025. [PubMed: 30853433]
53. Jia Y, Zhao Y, Kusakizako T, Wang Y, Pan C, Zhang Y, Nureki O, Hattori M, and Yan Z (2020). TMC1 and TMC2 Proteins Are Pore-Forming Subunits of Mechanosensitive Ion Channels. Neuron 105, 310–321 e313. 10.1016/j.neuron.2019.10.017. [PubMed: 31761710]
54. Tang YQ, Lee SA, Rahman M, Vanapalli SA, Lu H, and Schafer WR (2020). Ankyrin Is An Intracellular Tether for TMC Mechanotransduction Channels. Neuron 107, 759–761. 10.1016/j.neuron.2020.03.026. [PubMed: 32818474]
55. Marcovich I, and Holt JR (2020). Evolution and function of Tmc genes in mammalian hearing. Curr Opin Physiol 18, 11–19. 10.1016/j.cophys.2020.06.011.

56. Godt D, and Tepass U (1998). Drosophila oocyte localization is mediated by differential cadherin-based adhesion. Nature 395, 387–391. 10.1038/26493. [PubMed: 9759729]

57. Chanet S, and Huynh JR (2020). Collective cell sorting requires contractile cortical waves in germline cells. Current Biology 30, 4213–4226. 10.1016/j.cub.2020.08.045. [PubMed: 32916115]

58. Fettiplace R, and Kim KX (2014). The physiology of mechanoelectrical transduction channels in hearing. Physiol Rev 94, 951–986. 10.1152/physrev.00038.2013. [PubMed: 24987009]

59. Venkatachalam K, and Montell C (2007). TRP channels. Annu Rev Biochem 76, 387–417. 10.1146/annurev.biochem.75.103004.142819. [PubMed: 17579562]

60. Coste B, Mathur J, Schmidt M, Earley TJ, Ranade S, Petrus MJ, Dubin AE, and Patapoutian A (2010). Piezo1 and Piezo2 Are Essential Components of Distinct Mechanically Activated Cation Channels. Science 330, 55–60. 10.1126/science.1193270. [PubMed: 20813920]

61. Kim SE, Coste B, Chadha A, Cook B, and Patapoutian A (2012). The role of Drosophila Piezo in mechanical nociception. Nature 483, 209–212. 10.1038/nature10801. [PubMed: 22343891]

62. Amura CR, Marek L, Winn RA, and Heasley LE (2005). Inhibited neurogenesis in JNK1-deficient embryonic stem cells. Mol Cell Biol 25, 10791–10802. 10.1128/MCB.25.24.10791-10802.2005. [PubMed: 16314504]

63. Tiwari VK, Stadler MB, Wirbelauer C, Paro R, Schubeler D, and Beisel C (2012). A chromatin-modifying function of JNK during stem cell differentiation. Nat Genet 44, 94–100. 10.1038/ng.1036.

64. Agostini M, Romeo F, Inoue S, Niklison-Chirou MV, Elia AJ, Dinsdale D, Morone N, Knight RA, Mak TW, and Melino G (2016). Metabolic reprogramming during neuronal differentiation. Cell Death Differ 23, 1502–1514. 10.1038/cdd.2016.36. [PubMed: 27058317]

65. Zhang XD, Boyer L, Jin MJ, Mertens J, Kim YS, Ma L, Ma L, Hamm M, Gage FH, and Hunter T (2016). Metabolic reprogramming during neuronal differentiation from aerobic glycolysis to neuronal oxidative phosphorylation. Elife 5. 10.7554/eLife.13374.

66. Ulmer BM, Stoehr A, Schulze ML, Patel S, Gucek M, Mannhardt I, Funcke S, Murphy E, Eschenhagen T, and Hansen A (2018). Contractile Work Contributes to Maturation of Energy Metabolism in hiPSC-Derived Cardiomyocytes. Stem Cell Reports 10, 834–847. 10.1016/j.stemcr.2018.01.039. [PubMed: 29503093]

67. Karbassi E, Fenix A, Marchiano S, Muraoka N, Nakamura K, Yang X, and Murry CE (2020). Cardiomyocyte maturation: advances in knowledge and implications for regenerative medicine. Nature Reviews Cardiology 17, 341–359. 10.1038/s41569-019-0331-x. [PubMed: 32015528]

68. Peyronnet R, Nerbonne JM, and Kohl P (2016). Cardiac Mechano-Gated Ion Channels and Arrhythmias. Circulation Research 118, 311–329. 10.1161/CIRCRESAHA.115.305043. [PubMed: 26838316]

69. Grancharova T, Gerbin KA, Rosenberg AB, Roco CM, Arakaki JE, DeLizo CM, Dinh SQ, Donovan-Maiye RM, Hirano M, Nelson AM, et al. (2021). A comprehensive analysis of gene expression changes in a high replicate and open-source dataset of differentiating hiPSC-derived cardiomyocytes. Sci Rep-Uk 11. 10.1038/s41598-021-94732-1.

70. Gaio N, Martino A, Toth Z, Watson JT, Nicolaou D, and McBride-Gagyi S (2018). Masquelet technique: The effect of altering implant material and topography on membrane matrix composition, mechanical and barrier properties in a rat defect model. J Biomech 72, 53–62. 10.1016/j.jbiomech.2018.02.026. [PubMed: 29510858]

71. Ochiai H, Hayashi T, Umeda M, Yoshimura M, Harada A, Shimizu Y, Nakano K, Saitoh N, Liu Z, Yamamoto T, et al. (2020). Genome-wide kinetic properties of transcriptional bursting in mouse embryonic stem cells. Sci Adv 6, eaaz6699. 10.1126/sciadv.aaz6699. [PubMed: 32596448]

72. DeLuca SZ, and Spradling AC (2018). Efficient Expression of Genes in the Drosophila Germline Using a UAS Promoter Free of Interference by Hsp70 piRNAs. Genetics 209, 381–387. 10.1534/genetics.118.300874. [PubMed: 29669732]

73. Trcek T, Lionnet T, Shroff H, and Lehmann R (2017). mRNA quantification using single-molecule FISH in Drosophila embryos. Nat Protoc 12, 1326–1348. 10.1038/nprot.2017.030. [PubMed: 28594816]

74. Dupont G, Abou-Lovergne A, and Combettes L (2008). Stochastic aspects of oscillatory Ca^{2+} dynamics in hepatocytes. Biophys J 95, 2193–2202. 10.1529/biophysj.108.133777. [PubMed: 18515398]

75. Wu Y, Schellinger JN, Huang CL, and Rodan AR (2014). Hypotonicity stimulates potassium flux through the WNK-SPAK/OSR1 kinase cascade and the Ncc69 sodium-potassium-2-chloride cotransporter in the Drosophila renal tubule. J Biol Chem 289, 26131–26142. 10.1074/jbc.M114.577767. [PubMed: 25086033]

Highlights:

- Somatic cells encase and flatten the differentiating germline cysts
- The plasma membrane of germ cells in the flattened cysts is stretched
- Membrane stretching sustains the cytosolic Ca^{2+} level through the Tmc protein
- A CaMKI-Fray-JNK signaling relay mediates Ca^{2+}-dependent OXPHOS activation

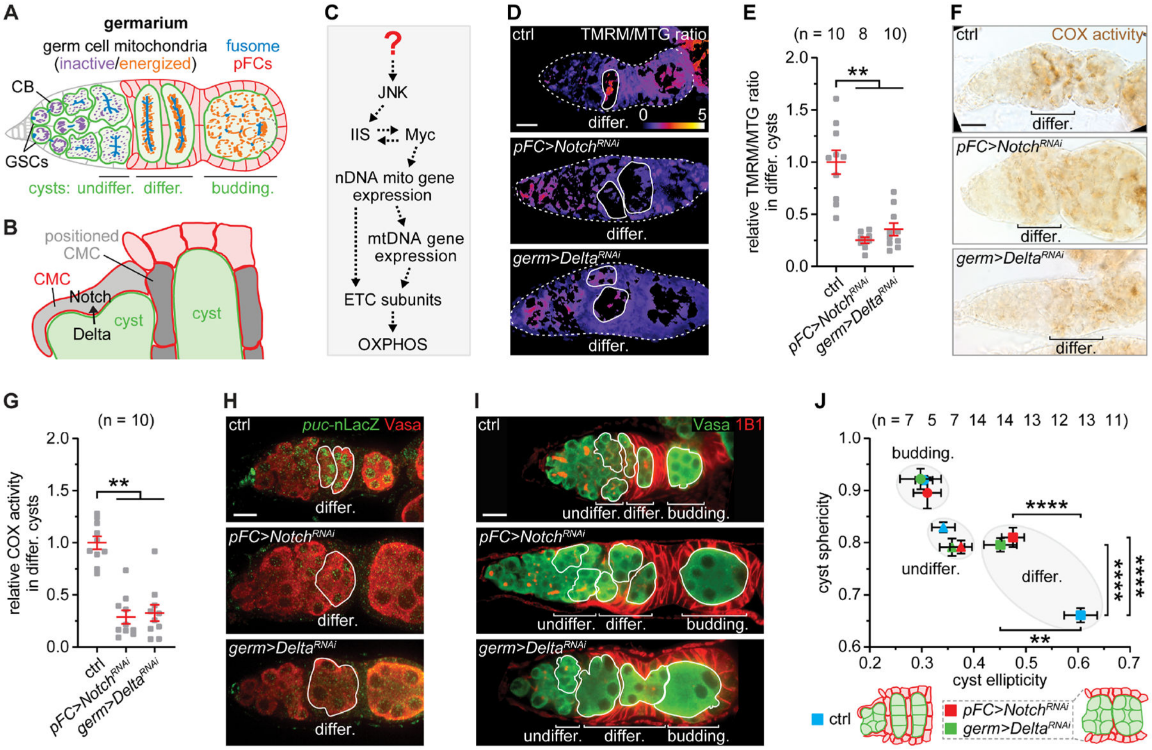

Figure 1. Cyst flattening drives JNK-mediated OXPHOS activation during differentiation.

(A) A schematic of a germarium showing germline stem cells (GSCs), cystoblasts (CB), pre-follicle cells (pFCs), undifferentiated cysts (undiffer.), differentiating cysts (differ.), and a budding egg chamber (budding.).

(B) A schematic showing that cross-migrating pFCs (CMCs) migrate alone the surface of a germline cyst (left cyst) under the control of the germline-to-soma Notch signaling and position themselves between germline cysts.

(C) A signaling relay coordinates the expression of mitochondrial genes encoded on both the nuclear genome (nDNA) and mtDNA to promote OXPHOS activation in differentiating cysts. IIS, Insulin/IGF-1 signaling.

(D) Representative ratiometric images of TMRM and MitoTracker Green (MTG) double staining in ctrl, *pFC>Notch* RNAi, and *germ>Delta* RNAi germaria.

(E) Quantification of TMRM/MTG ratio as an indication of inner mitochondrial membrane potential in differentiating cysts from ctrl (n=10), *pFC>Notch* RNAi (n=8), and *germ>Delta* RNAi (n=10) germaria.

(F) Representative images of ctrl, *pFC>Notch* RNAi, and *germ>Delta* RNAi germaria stained for COX activity.

(G) Quantification of COX activity in differentiating cysts from ctrl, *pFC>Notch* RNAi, and *germ>Delta* RNAi germaria. n = 10 germaria for each genotype.

(H) Expression of *puc*-nLacZ (JNK activity reporter) in ctrl, *pFC>Notch* RNAi, and *germ>Delta* RNAi germaria.

(I) Germaria of ctrl, *pFC>Notch* RNAi, or *germ>Delta* RNAi stained for Vasa and 1B1.

(J) Sphericity and ellipticity of developing cysts. The numbers (n) of cysts for each developmental stage and genotype are indicated. Note that pFCs are not located between differentiating cysts when the germline-to-soma Notch signaling is suppressed.

pFC>Luciferase RNAi was used as the control in all panels. Bars represent mean ± SEM. $**P < 0.01$ and $****P < 0.0001$. Scale bars, 10 μm.

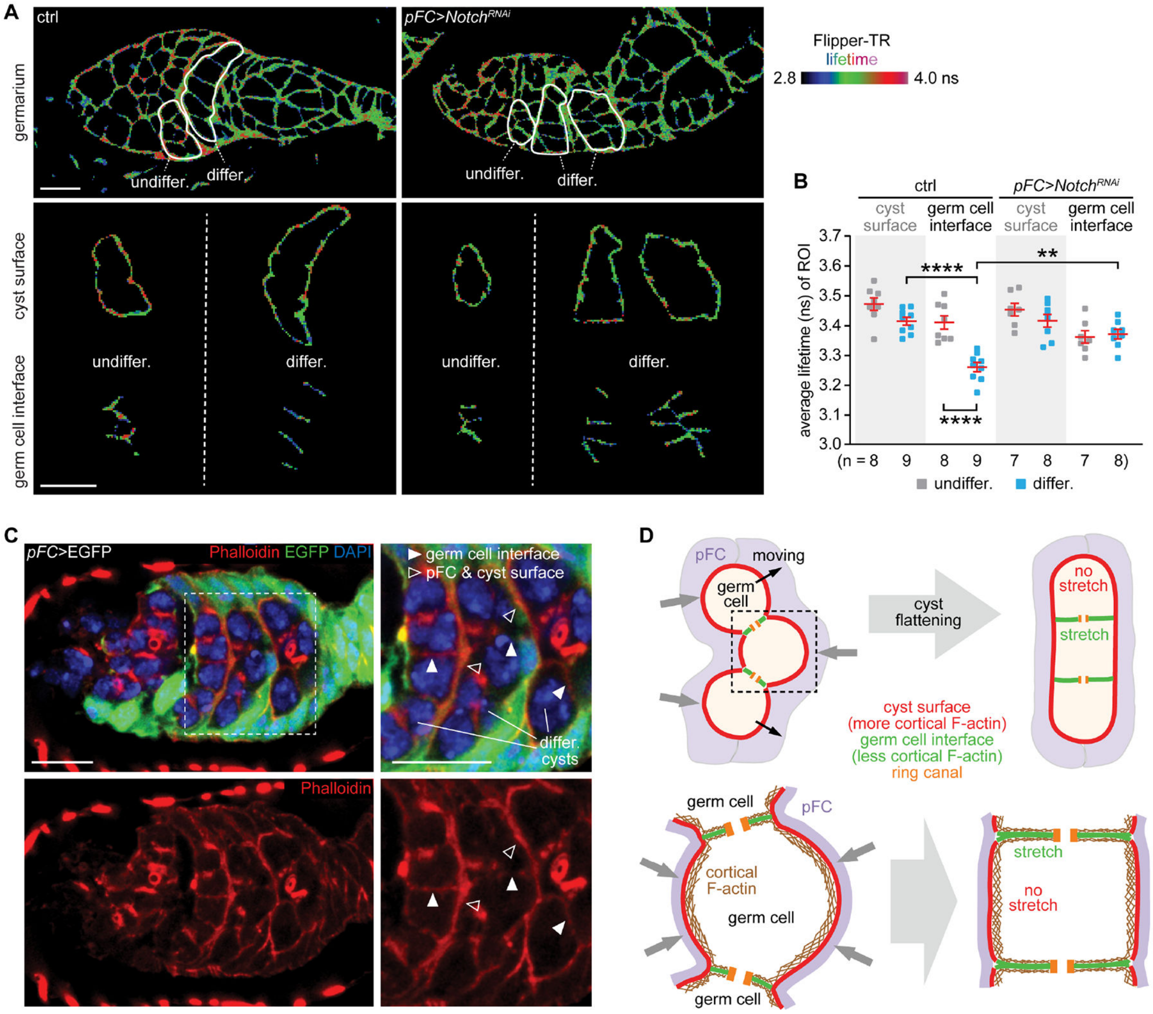

Figure 2. Membranes at the germ cell interfaces are stretched in the flattened differentiating cysts.

(A) Representative images of Flipper-TR lifetime on cell membranes in germaria of ctrl or *pFC>Notch* RNAi. Note that shortened Flipper-TR lifetimes (bluish pixels) correspond to increased membrane expansion. The upper panels are lifetime images of whole germaria, with cysts at different developmental stages outlined. The lower panels are cropped images of surfaces and germ cell interfaces of the outlined cysts in the upper panels.

(B) Quantification of average Flipper-TR lifetimes in regions of interest (ROIs) of ctrl or *pFC>Notch* RNAi germaria. The numbers (n) of ROIs are indicated.

(C) Representative images of a germarium expressing EGFP in pFCs. Enlarged view of outlined areas are shown on the right.

(D) The proposed model illustrating that the flattening of a differentiating cyst results in increased membrane tension at the germ cell interfaces, but not at the cyst surface. The dashed box outlines a germ cell. The changes in germ cell mechanics during cyst flattening are illustrated in the lower panel. The cell membranes (red, cyst surface regions) are pushed by neighboring pFCs (purple). As phospholipid fluidity and membrane area changes are restricted by the actin cortex, forces exerted on these membranes (red, cyst surface regions) would be transmitted to the membranes at the germ cell interfaces (green), leading to their expansion.

pFC>Luciferase RNAi was used as the control. Bars represent mean ± SEM. $^{**}P < 0.01$ and $^{****}P < 0.0001$. Scale bars, 10 μm.

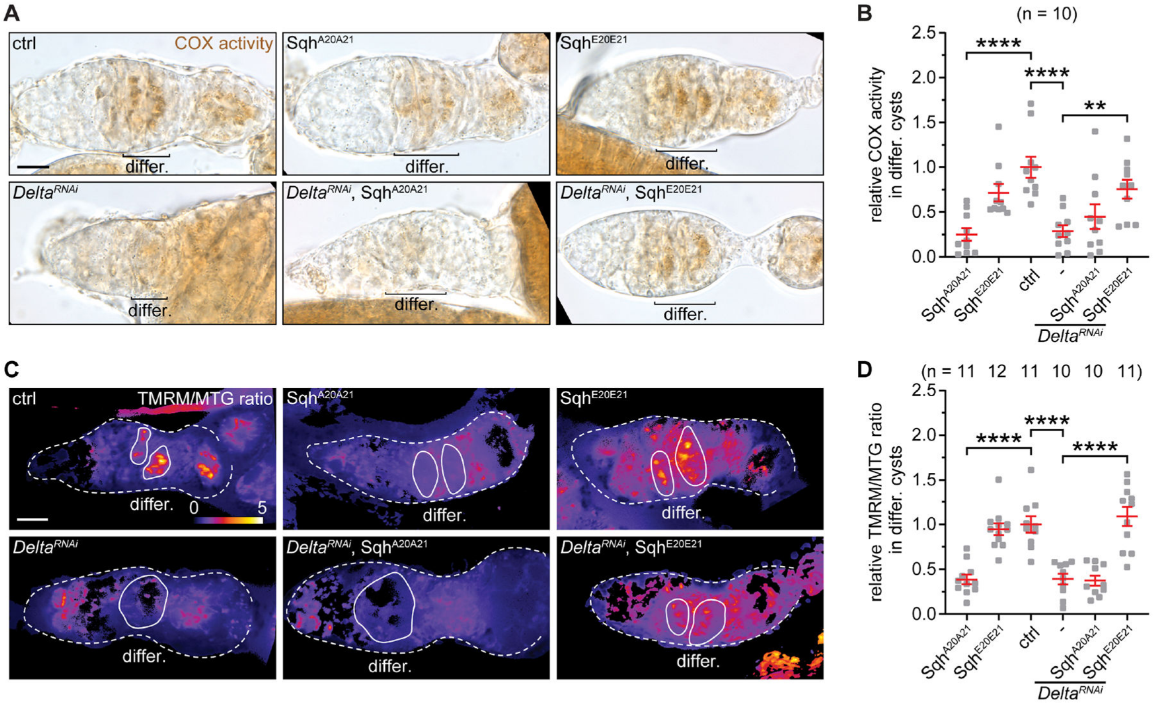

Figure 3. OXPHOS activation in differentiating cysts requires increased membrane stretching.

(A) Representative images of germaria with indicated genotypes stained for COX activity.

(B) Quantification of COX activity in differentiating cysts with indicated genotypes. n = 10 germaria for each genotype.

(C) Ratiometric images of TMRM and MTG in germaria with indicated genotypes.

(D) Quantification of TMRM/MTG ratio in differentiating cysts with indicated genotypes. The numbers (n) of cysts for each genotype are indicated.

germ>Luciferase RNAi was used as the control for all panels. Bars represent mean ± SEM. $^{**}P < 0.01$ and $^{****}P < 0.0001$. Scale bars, 10 μm.

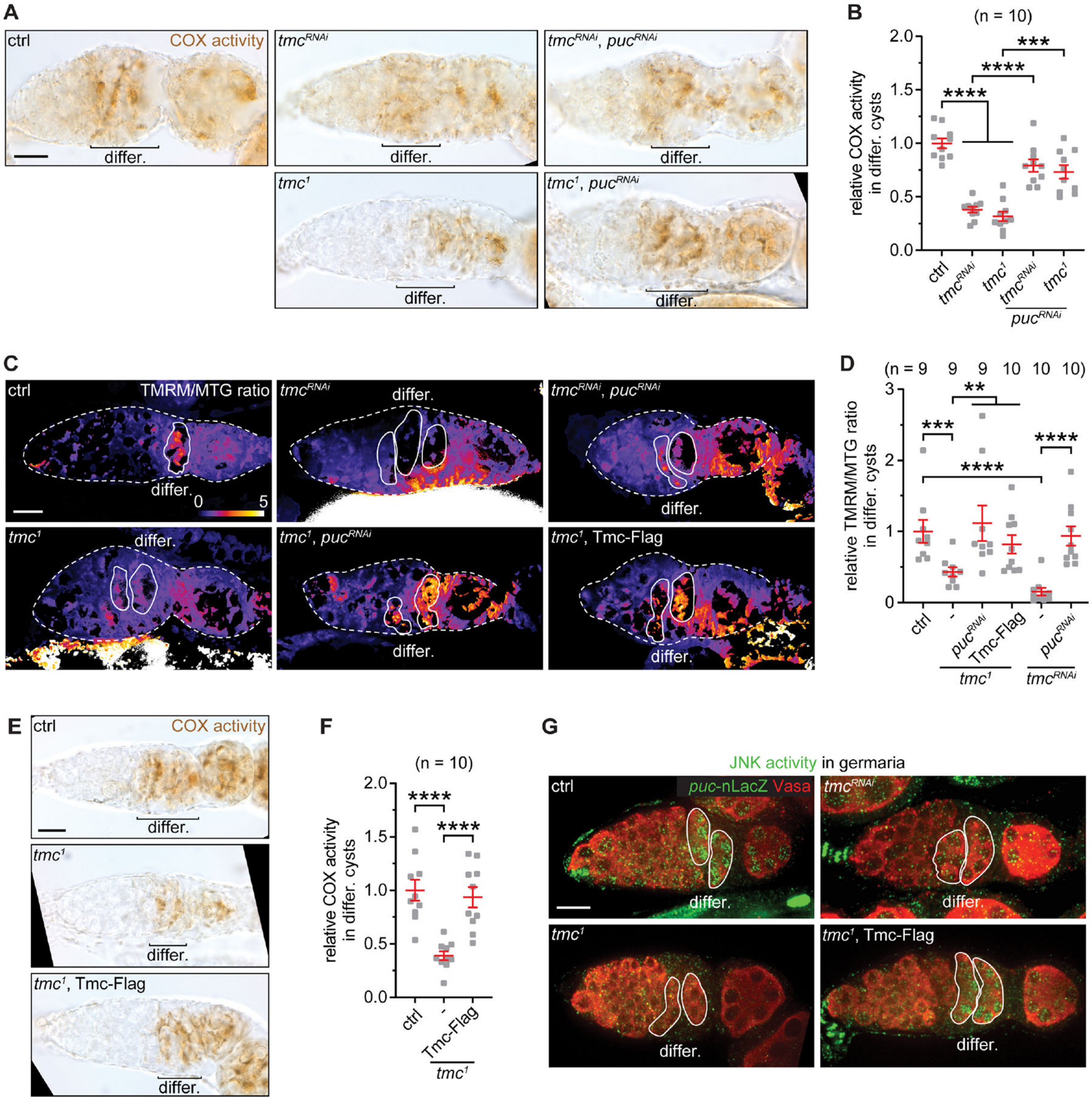

Figure 4. Tmc is required for OXPHOS activation in differentiating cysts.

(A) Representative images of germaria with indicated genotypes stained for COX activity.

(B) Quantification of COX activity in differentiating cysts with indicated genotypes. n = 10 germaria for each genotype.

(C) Ratiometric images of TMRM and MTG double staining in germaria with indicated genotypes.

(D) Quantification of TMRM/MTG ratio in differentiating cysts with indicated genotypes. The numbers (n) of cysts for each genotype are indicated.

(E) Representative images of germaria with indicated genotypes stained for COX activity.

(F) Quantification of COX activity in differentiating cysts with indicated genotypes. n = 10 germaria for each genotype.

(G) Expression of *puc*-nLacZ (JNK activity reporter) in germaria with indicated genotypes.

germ>Luciferase RNAi was used as the control. Bars represent mean ± SEM. $^{**}P < 0.01$, $^{***}P < 0.001$, and $^{****}P < 0.0001$. Scale bar, 10 μm.

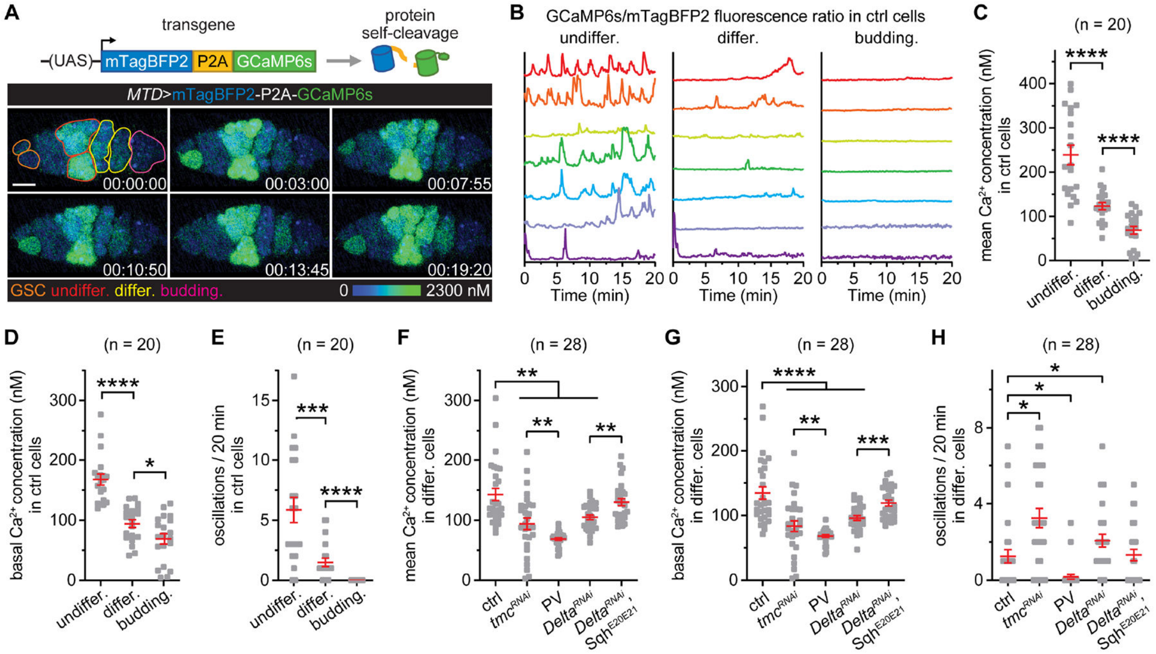

Figure 5. Tmc maintains cytosolic Ca^{2+} concentration in differentiating cysts.

(A) A schematic of the Ca^{2+} reporter, UASz-mTagBFP2-P2A-GCaMP6s, and a live recording that shows Ca^{2+} levels and oscillations in germline cysts at different stages (colored outlines). Time stamp in h:min:s. *MTD-Gal4* was used to drive germline expression of the Ca^{2+} reporter. The range of intracellular Ca^{2+} concentrations is shown.

(B) Representative traces of GCaMP6s/mTagBFP2 fluorescence ratio in individual germ cells from 5 germaria at different developmental stages.

(C-E) Mean and basal Ca^{2+} concentrations, and Ca^{2+} oscillation frequency in individual germ cells from 5 ctrl germaria.

(F-H) Mean and basal Ca^{2+} concentrations, and Ca^{2+} oscillation frequency in individual differentiating cells with indicated genotypes. n = 28 cells from 7 germaria for each genotype.

Bars represent mean ± SEM. $^{*}P < 0.05$, $^{**}P < 0.01$, $^{***}P < 0.001$, and $^{****}P < 0.0001$. Scale bar, 10 μm.

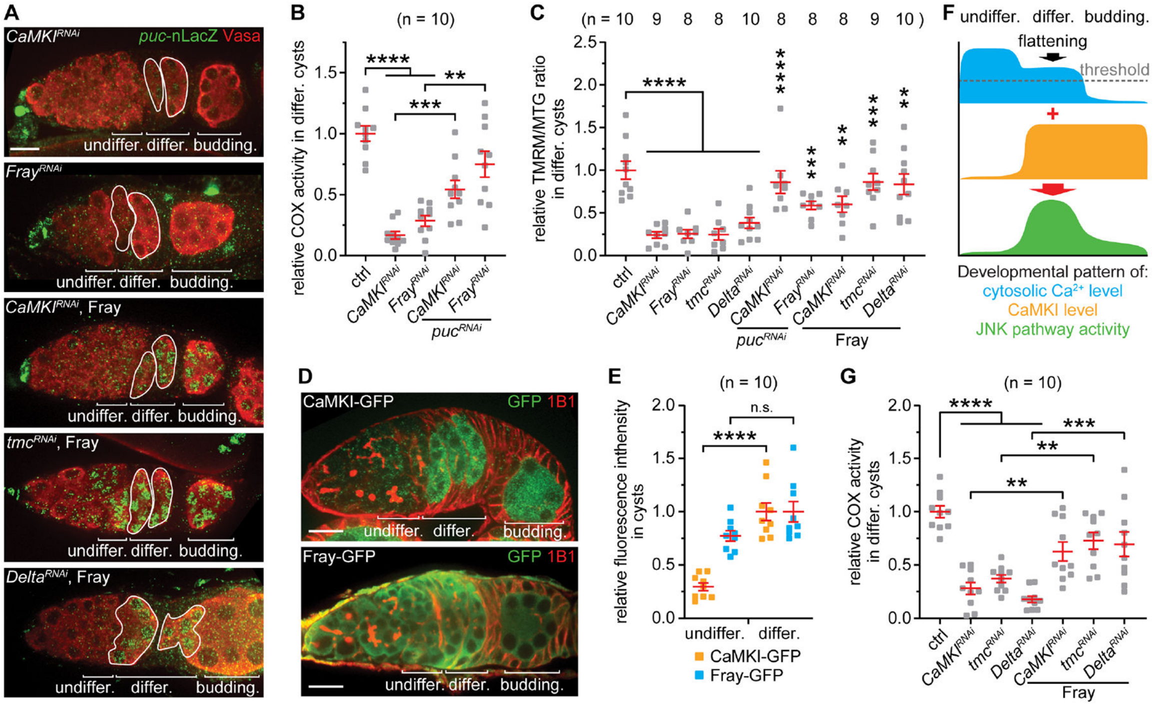

Figure 6. Cytosolic Ca^{2+} triggers OXPHOS activation in differentiating cells through CaMKI and Fray.

(A) Expression of *puc*-nLacZ (JNK activity reporter) in germaria with indicated genotypes.

(B) Quantification of COX activity in differentiating cysts from germaria with indicated genotypes. n = 10 germaria for each genotype.

(C) Quantification of TMRM/MTG ratio in differentiating cysts with indicated genotypes. The numbers (n) of cysts for each genotype are indicated.

(D) Representative images of endogenous expression of CaMKI-GFP and Fray-GFP in germaria.

(E) Quantification for the expression levels of CaMKI-GFP and Fray-GFP in germline cysts. n = 10 germaria for each protein.

(F) The developmental patterns of cytosolic Ca^{2+}, CaMKI expression, and JNK pathway activity during germline cyst differentiation. The onset of CaMKI expression in differentiating cysts restricts Ca^{2+}-dependent JNK activation at this stage.

(G) Quantification of COX activity in differentiating cysts with indicated genotypes. n = 10 germaria for each genotype.

Bars represent mean ± SEM. $*P < 0.05$, $**P < 0.01$, $***P < 0.001$, and $****P < 0.0001$. Scale bars, 10 μm.

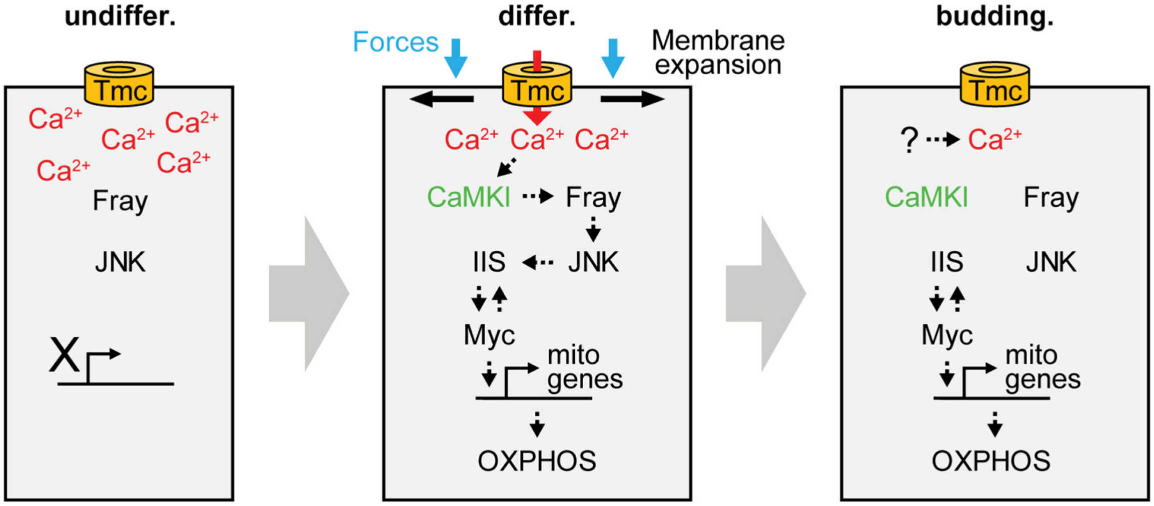

Figure 7. A schematic of the mechanotransduction pathway that activates OXPHOS during ovarian cyst differentiation.

In flattened differentiating cysts, Tmc-mediated Ca^{2+} influx maintains cytosolic Ca^{2+} levels in response to cell membrane stretching, which activates JNK through CaMKI and Fray. JNK initiates an IIS-Myc feedforward loop that induces the transcription of mitochondrial genes, resulting in the activation of OXPHOS. Undifferentiated cysts have high concentration of cytosolic Ca^{2+} that is independent of Tmc, but low JNK activity due to the lack of CaMKI expression. In budding egg chamber cysts, JNK is inactive due to reduced cytosolic Ca^{2+} concentrations. However, the IIS-Myc feedforward loop is established and maintains ETC biogenesis until later stages.

KEY RESOURCES TABLE

REAGENT or RESOURCE
Antibodies
Rabbit anti-Vasa
Rabbit anti-GFP
Mouse anti-Orb
Mouse anti-Hts
Mouse anti-β-galactosidase
Mouse anti-FLAG
Alexa Fluor 568 donkey anti-rabbit IgG
Alexa Fluor 568 goat anti-mouse IgG
Alexa Fluor 488 goat anti-rabbit IgG
Alexa Fluor 488 goat anti-mouse IgG
Bacterial and virus strains
NEB® 5-alpha Competent E. coli
Chemicals, peptides, and recombinant proteins
Paraformaldehyde 16% Solution
Triton X-100
Schneider's *Drosophila* Medium
DAPI
Flipper-TR fluorescent tension probe
Cytochrome c from equine heart
Catalase from bovine liver
TMRM
MitoTracker Green
Alexa Fluor 568-Phalloidin
3,3'-Diaminobenzidine tetrahydrochloride
Antimycin A
Sodium malonate dibasic monohydrate
Rotenone
Digitonin

REAGENT or RESOURCE
3-(trimethoxysilyl) propyl methacrylate
PEG-DA hydrogel solution
Irgacure 2959
Proteinase K
Heparin ammonium salt
Salmon Sperm DNA
Dextran sulfate sodium salt
Critical commercial assays
In-Fusion® HD Cloning Kit
Calcium Calibration Buffer Kit #1
Effectene Transfection Reagent
Experimental models: Cell lines
Drosophila S2 cells
Experimental models: Organisms/strains
D. melanogaster: w ^{1118}
D. melanogaster: Luciferase RNAi
D. melanogaster: 109–30-Gal4
D. melanogaster: nos-Gal4
D. melanogaster: nos-Gal4
D. melanogaster: UAS-2×EGFP
D. melanogaster: MTD-Gal4
D. melanogaster: puc-lacZ$^{A251.1F3}$
D. melanogaster: NRE-EGFP
D. melanogaster: Notch RNAi
D. melanogaster: Delta RNAi

REAGENT or RESOURCE
D. melanogaster: UASp-Sqh^{A20A21}
D. melanogaster: UASp-Sqh^{E20E21}
D. melanogaster: tmc^{1}
D. melanogaster: tmc RNAi
D. melanogaster: puc RNAi
D. melanogaster: JNK RNAi
D. melanogaster: MCU RNAi
D. melanogaster: CaMKI RNAi
D. melanogaster: CaMKI RNAi #2
D. melanogaster: fray RNAi
D. melanogaster: fray RNAi #2
D. melanogaster: Myc-GFP
D. melanogaster: CaMKI-GFP
D. melanogaster: Fray-GFP
D. melanogaster: RNAi stains for candidate RNAi screen, see Supplemental Table 1 and 2
D. melanogaster: pUASz-mTagBFP2-P2A-GCaMP6s
D. melanogaster: pUASz-mTagBFP2
D. melanogaster: pUASz-Parvalbumin-3xHA
D. melanogaster: pUASz-Fray-3xHA
D. melanogaster: pUASz-Tmc-Falg

REAGENT or RESOURCE
Oligonucleotides
mTagBFP2-F ATGGTGTCTAAGGGCGAAGAGC
mTagBFP2-P2A-R GGGGCCGGGGTTCTCCTCCACGTCGCCGGCCTGCTTCAGCAGGGAGAAGTTGGTGGCGCCATTAAGCTTGTGCCCCAGTTTGCTA
GCaMP6s-F GAGAACCCCGGCCCCATGGTCGACTCATCACGTCGTAAG
GCaMP6s-R TCACTTCGCTGTCATCATTTGTACAAAC
Tmc-F TCAAAGGATCCCTCGAGATGCAGAGCAGCGCCGATGC
Tmc-Flag-R CTAGTGGTACCCTCGAGCTACTTATCGTCGTCATCCTTGTAGTCCATTTTCTCATGCTCATTTTCAATGTCAATCCTTATAATG
PV-F ATGGCCCAGGTGCAGCTGC
PV-3xHA-R TTAAGCGTAATCTGGAACGTCATATGGATAGGATCCTGCATAGTCCGGGACGTCATAGGGATAGCCCGCATAGTCAGGAACATCGTATGGATAGCCTCCACCTGCGG
Fray-F ATGACCTCCATACCCGCCAATC
Fray-3xHA-R TTAAGCGTAATCTGGAACGTCATATGGATAGGATCCTGCATAGTCCGGGACGTCATAGGGATAGCCCGCATAGTCAGGAACATCGTATGGATAGCCTCCACCGTCCG
Fluorescently labelled DNA probes for *JNK-RB:* TCGACGGTGTAGTGTTGGTGTGTGGATGGTGAAGTTGGTGTGGGCCGTAGATTAATGTACGCATACTATTCCTTGGGCACGGGTGATAGTATCGTAAGCGGTTTCTT
Fluorescently labelled DNA probes for *Tmc-RD 1*: TTTGTAGAATTCCCTCTTGGTTCAGTTCGTAGGATCTGTGCTCTGGTTTTGCAATGGGAAGAAATTGTGTAGCTCTCCTCTGTCGTATAGACACTGGAGCCAGGCGG
Fluorescently labelled DNA probes for *Tmc-RD 2:* CTAAGTCGTCTGAGTCTTTCTAGTCGTGGTTCGATATCTCTGAATCAGTGGAACTCTCCGTGTCGAAGGCATTGGTAGTGGTGGTGTATTCATCTTCTTCCCACATAC
Recombinant DNA
pUASZ-1.0
pCMV-PV-GFP
pFLC-I-RE53265
pUASt-Tmc
Software and algorithms
Imaris
FIJI / ImageJ
Origin 2021
Las X software
Interactive Data Language

REAGENT or RESOURCE
Prism 9
Deposited data
Original images and Graph pad files
Other
Chamlide chamber
Nunc™ Lab-Tek™ chambered coverglass